J. Mech. Phys. Solids 208 (2026) 106461

Contents lists available at ScienceDirect

Journal of the Mechanics and Physics of Solids

journal homepage: www.elsevier.com/locate/jmps

The broad wrinkling landscape of hyperelastic parallelogram-shaped membranes: From wrinkle migration to restabilization and their subsequent reappearance elsewhere

Mohammad Hosein Nejabatmeimandi [a,b], Francesco Dal Corso [a,*]

[a] DICAM, University of Trento, via Mesiano 77, Trento, I-38123, Italy
[b] Tensys Ltd, 122 Wells Rd, Bath, UK

ARTICLE INFO

Keywords:
Self-restabilization
Quasi-rectangular membranes
Wrinkling pattern morphing
Perturbation approach

ABSTRACT

Wrinkling is a commonly observed out-of-plane instability in membrane structures due to their extremely low bending-to-stretching stiffness ratio. It has been extensively investigated for symmetric membrane geometries and boundary conditions that induce planar non-uniform stress states by preventing the lateral contraction at the edges, and is also known to potentially display self-restabilization. This study investigates an initially flat, parallelogram-shaped hyperelastic membrane, focusing on the effect of the inclination angle that defines its deviation from rectangular geometry. It is shown that wrinkling can occur either centrally or at the two opposite obtuse-angled corners–even for small inclination angles–during stretching with unconstrained lateral contraction, a condition under which the flat configuration for the rectangular counterpart remains always stable. Three distinct evolutions of the wrinkling pattern are numerically identified, all ultimately leading to corner-localized wrinkles. This final state may arise (i) directly, without a prior bifurcation, or after the appearance of central wrinkling that either (ii) restabilizes or (iii) separates and migrates toward the corners. A closed-form expression for the critical wrinkling condition is derived by combining a perturbation approach with an energy-based method in the framework of linear elasticity. This provides an accurate estimate of the onset and pattern of central wrinkling. The present findings reveal new pathways in wrinkling pattern evolution and introduce a novel approach to unconventional boundary-value problems, with potential applications ranging from lightweight structural systems to flexible electronics.

1. Introduction

Thin membranes and films are highly flexible bi-dimensional structures abundant in nature (cells, insect wings, and leaves) and widely manufactured for diverse engineering applications–including architecture, aerospace, electronics, and medicine–due to their lightweight and adaptable nature. These structures offer mechanically efficient and aesthetically appealing solutions for applications spanning from covering of large spaces (Comitti et al., 2024) to hosting electronic components in flexible devices (Landis et al., 2022). Their extremely low bending-to-stretching stiffness ratio however facilitates the onset of structural elastic instabilities, posing a significant challenge by compromising both structural integrity and visual appeal. Among the possible instabilities, membranes are particularly prone to wrinkling, exhibiting a sinusoidal-like out-of-plane displacement on the surface, with a short wavelength aligned

* Corresponding author.
E-mail address: francesco.dalcorso@unitn.it (F. Dal Corso).

https://doi.org/10.1016/j.jmps.2025.106461
Received 29 April 2025; Received in revised form 7 October 2025; Accepted 28 November 2025
Available online 4 December 2025

to the direction of the principal compressive stress, creating localized curvature. Wrinkling is commonly experienced in everyday life with items like plastic wraps, clothing fabrics, curtains, and balloons.

State of the art. Tension-field theory, initially developed in 1929 (Wagner, 1929) and later extended (Reissner, 1938), has been the foundational framework for analyzing wrinkling instability in thin-walled structures. This two-dimensional nonlinear model assumes that wrinkles have infinitesimal wavelengths, with the material being considered to have no compressive bearing capacity. However, despite several enhancements (Stein and Hedgepeth, 1961; Coman, 2007) and generalizations (Danielson and Natarajan, 1975; Steigmann, 1990; Pipkin, 1986), tension-field theory still faces limitations, particularly in its neglect of bending energy (Damil et al., 2013). Consequently, researchers have increasingly turned attention to more advanced plate and shell models that account for both stretching and bending effects, such as the Föppl–von Kármán model and its extended version, the latter taking into account the large in-plane deformations of the membrane. Through these models, the analysis of thin sheets gained more precision also in terms of predicting the post-critical response and the corresponding wrinkling morphology.

Deep insights into the wrinkling mechanisms have then been gained in several different setups, mainly restricted to axial or axis symmetry conditions. As expected, the position of wrinkling within a membrane changes with variations in the membrane geometry and loading conditions. Wrinkling may be spread over the whole membrane, as under shear loading (Wong and Pellegrino, 2006a), or emerges as an isola-center bifurcation in the two-axis symmetric problem of a stretched rectangular membrane with constrained lateral contraction at the edges (Ishida et al., 2024; Suñé et al., 2023; Wang et al., 2023). Localized wrinkling can also occur near the membrane's free edge, with wrinkles oriented orthogonally to the boundary, as observed in elastic plate stamping (Hure et al., 2012), elastically supported, prestressed incompressible isotropic plates (Destrade et al., 2016), spinning elastic membranes (Coman, 2023), and membranes under pressure loading (Coman and Bassom, 2016). Alternatively, wrinkles may appear close to and align parallel to the free edge, particularly in twisted, pre-stretched membranes (Wang et al., 2023). Edge wrinkling has also been investigated as instability patterns in growing curled petals and leaves (Wang et al., 2024).

In the context of inelastic membrane behaviour, the Mullins effect has been shown to induce a distinctive wrinkling response: while no wrinkles appear during the initial loading, they emerge during the first unloading and persist throughout all subsequent loading cycles (Fehér et al., 2018).

Drawing an analogy with the restabilization of the trivial path observed in variable-length rods under compression (Bigoni et al., 2014; Bosi et al., 2016), both theoretical and experimental investigations of highly stretched, initially isotropic thin sheets have revealed a surprising restabilization phenomenon (Fu et al., 2021, 2019; Healey et al., 2013; Li and Healey, 2016; Nayyar et al., 2011; Steigmann, 2013; Taylor et al., 2014; Yang et al., 2022; Zheng, 2009). In this context, wrinkle amplitude initially increases with stretching but subsequently diminishes as stretching continues, eventually vanishing entirely–thereby demonstrating a recovery of stability of the flat configuration. Such a restabilization phenomenon has been also addressed in orthotropic (Liu et al., 2019; Sipos and Fehér, 2016) and anisotropic (Fu et al., 2022) membranes, as well as in soft shells (Wang et al., 2020). A recent analysis for anisotropic membrane has also disclosed the possibility of wrinkling reappearance at the same central location after its disappearance due to restabilization (Chai et al., 2024).

Wrinkling instability has been also studied in membranes attached to a substrate, showing wrinkling patterns in trapezoidal film/substrate bilayers (Xu et al., 2017), characterized by period doubling (Xu et al., 2015), with axisymmetric/diamond-like mode transition (Xu and Potier-Ferry, 2016), with hexagonal geometry in spheres and toroids with an elastic core (Brojan et al., 2015; Jiménez et al., 2016; Stoop et al., 2015; Wang et al., 2025), with smooth-wrinkle-ridge-sagging transitions (Ding et al., 2021), with crystallography on spherical surfaces (Brojan et al., 2015), and in differentially growing bilayers (Shen et al., 2024).

Owing to the complexity of stress fields within membranes and the potential involvement of nonlinearities, only a limited number of studies have produced closed-form analytical solutions for predicting the critical conditions for wrinkling and the resulting patterns. The observation of stretch-induced wrinkling in rectangular sheets (Friedl et al., 2000) thus motivated simplified buckling models for complex stress states lacking direct analytical solutions. Scaling laws for wrinkle wavelength and amplitude have been established through energy minimization (Cerda and Mahadevan, 2003; Cerda et al., 2002; Mirandola et al., 2023; Vandeparre et al., 2011), and energy-based models for wavelength selection have been proposed (Jacques and Potier-Ferry, 2005). Furthermore, the dependence of critical wrinkling strain on aspect ratios has validated scaling relationships between applied stretch and wrinkling behaviour (Cerda et al., 2002; Kim et al., 2012; Puntel et al., 2011). Finally, the transition between periodic wrinkling and global buckling has been analytically predicted for a thin elastic ring bound to an equally curved 2D substrate that contains an inner cavity (Lagrange et al., 2016).

The deep understanding of wrinkling mechanisms unlocked innovative applications across several technological fields. Recent advancements have leveraged the unique properties of wrinkling in auxetic membranes and nematic elastomer sheets to achieve on-demand, non-standard wrinkling patterns, suppressing unwanted instabilities through microstructure formation (Plucinsky and Bhattacharya, 2017; Venkata et al., 2023). These developments are critical for lightweight deployable space structures, such as solar sails and antennas, where precise control of membrane behaviour enhances performance (Ishida et al., 2024). In terrestrial applications, wrinkling informs the design of complex fabric roofs and smart mechanical devices, including dielectric elastomeric layers and bilayer gel beams, where controlled instabilities enable structural morphing, sensing, and actuation in biomedical and soft robotics contexts (Nardinocchi and Puntel, 2017).

For a further detailed overview of tension-induced film wrinkling, readers are directed to the review by Wang et al. (2022).

Article contribution. The mechanics and wrinkling instability of an unconventional class of two-dimensional structures–specifically, initially flat, parallelogram-shaped hyperelastic membranes–are investigated under a stretching process that allows lateral contraction.

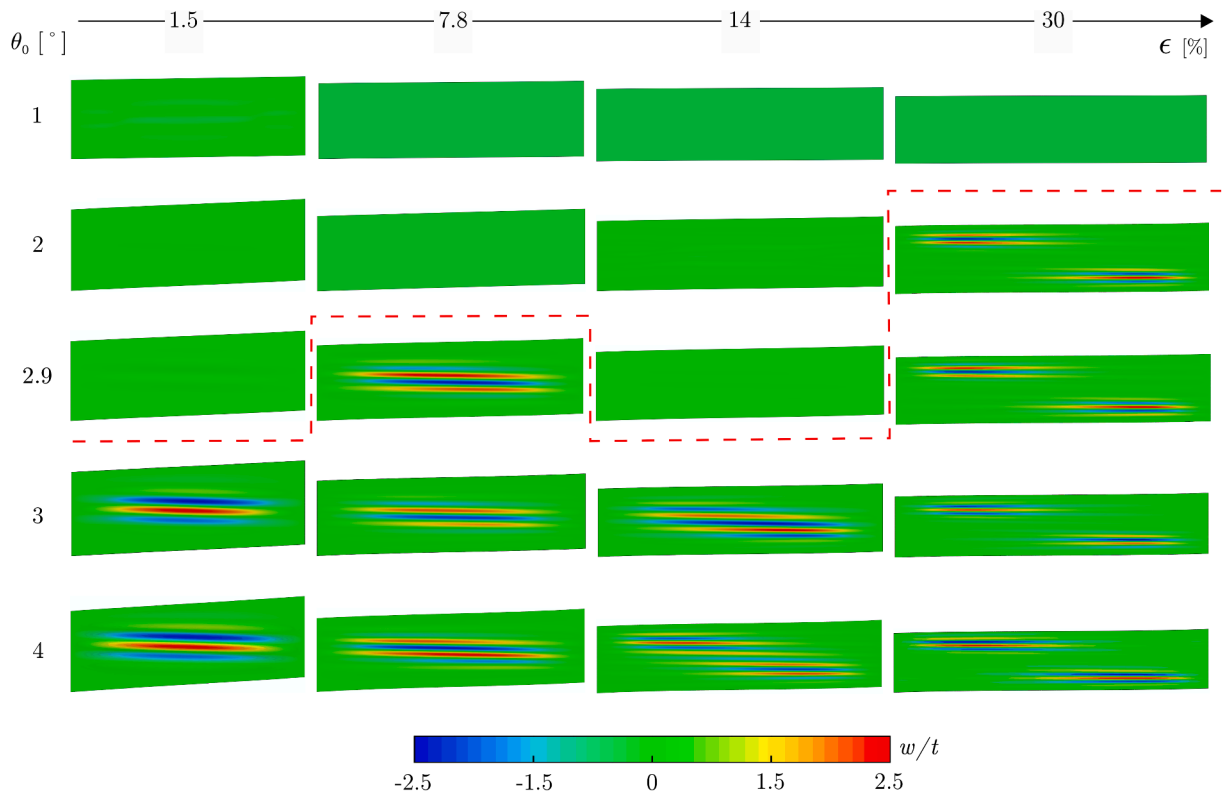

Fig. 1. Maps of the out-of-plane displacement w, normalized through division by the membrane thickness t, showing the wrinkling pattern evolution at four stages of increasing elongation strain $\epsilon = \{1.5, 7.8, 14, 30\}\%$. The maps are obtained from Finite Element simulations for five compressible Neo-Hookean membranes with the same width-to-thickness ratio $\alpha = 1500$ and (in-plane) aspect ratio $\beta = 3$, but differing in the initial inclination angle θ_0 defining the undeformed parallelogram shape. Homogeneous (green) color implies a planar state while inhomogeneous color shows the wrinkling pattern, which appears aligned parallel with the elongation direction. In addition to the case ($\theta_0 = 1°$) that shows no out-of-plane displacement at every deformation stage, three different types of evolutions are shown, all ending with wrinkle close to the two obtuse-angled corners.

In comparison with the usual setups analyzed in wrinkling problems, besides removing the edge constraint of zero lateral contraction, the investigated boundary-value problem is also less symmetric, as it has a rotational symmetry of order 2, and it allows refined tuning of the inhomogeneity level of the mechanical fields through the inclination angle θ_0, which quantifies the deviation of the undeformed parallelogram shape from the rectangular geometry ($\theta_0 = 0$). The inhomogeneous fields and wrinkling phenomena are investigated for varying initial inclination angle θ_0 and the in-plane aspect ratio β. By contrast to the limiting case of a rectangular membrane allowed to laterally contract under elongation–for which the stress field remains purely uniaxial under tension, and no compressive stresses arise during elongation, thereby precluding instability–it is shown that introducing an inclination angle generates a compressive principal stress component, which can induce wrinkling even for small deviations ($|\theta_0| \ll 1$) from the rectangular configuration.

Finite Element analyses reveal that when wrinkling appears, it develops either in the central region of the membrane or close to the two obtuse-angled corners, Fig. 1. More specifically, three distinct evolutions of the wrinkling pattern are identified, all ultimately leading to the appearance of wrinkles at the corners. The key difference between these evolutions lies in the behaviour prior to this final state: central wrinkling may either not appear at all (case $\theta_0 = 2°$ in Fig. 1) or manifest during an earlier stage of deformation. In the latter case, it either restabilizes (through a complete wrinkling disappearance, case $\theta_0 = 2.9°$ in Fig. 1) or separates and migrates toward the two corners (cases $\theta_0 = 3°$ and $4°$ in Fig. 1) as the elongation strain ϵ increases.

The numerical analysis is complemented by an analytical treatment within a linear elasticity framework. Using a perturbation approach based on small values of the initial inclination angle θ_0, a second-order expansion of the stress field is derived. This analysis identifies the cause of potential central wrinkling formation as a second-order compressive principal stress within the parallelogram membrane. A relatively simple closed-form expression is finally obtained for evaluating the critical elongation strain and the central wrinkling pattern by considering the approximated stress fields within an energy principle. The analytical expression is shown to successfully predict the wrinkling condition disclosed through Finite Element simulations with varying of the parallelogram membrane geometry, Fig. 2.

Article outline. The geometrically extended version of the Föppl–von Kármán model is recalled in Section 2, along with the derivation of the constitutive relations for specific choices of classical hyperelastic materials and a description of the membrane geometry and boundary conditions. Details of the Finite Element analyses, numerical results for the planar response, critical conditions, post-critical

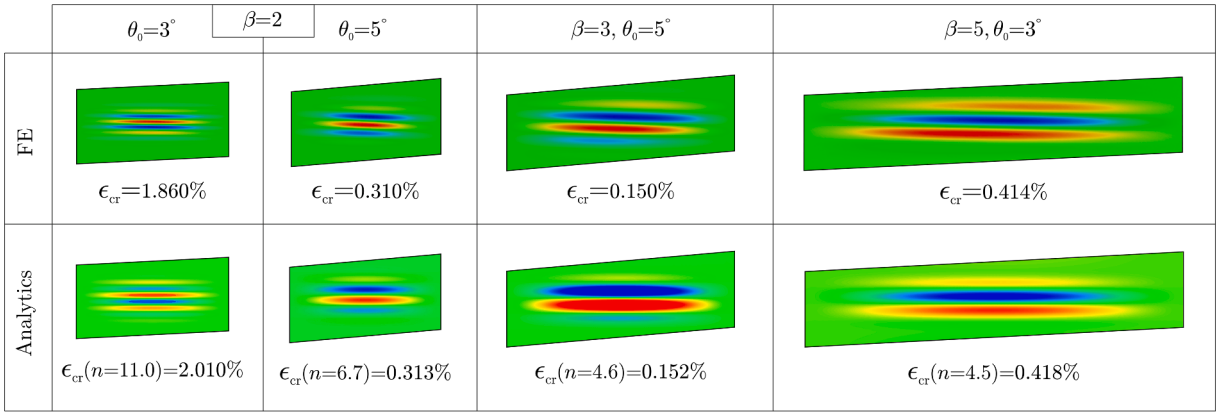

Fig. 2. Comparison of the out-of-plane displacement maps, disclosing the wrinkling pattern for $\beta = 2$ and $\theta_0 = 3°$ and 5°, for $\beta = 3$ and $\theta_0 = 5°$, and for $\beta = 5$ and $\theta_0 = 5°$. An excellent agreement is found between the patterns from finite element (FE) simulations (above) and from the analytical approach (bottom) in terms of either the critical elongation strain ϵ_{cr} and of the wrinkling pattern. The corresponding analytical prediction of the critical elongation strain ϵ_{cr} is also reported by highlighting the minimizing positive value of n defining the wrinkling ansatz, Eq. (68).

response, and wrinkling pattern evolution, along with the related discussion, are provided in Section 3. The perturbation approach is applied in Section 4 to obtain an approximated analytical description of the planar stress fields, which is in turn used into the energy approach to evaluate closed-form expressions for predicting the critical elongation strain of wrinkling and its pattern. The results in terms of both the planar stress field description and the critical deformation and mode are successfully validated through comparison with the numerical predictions. Concluding remarks are finally provided in Section 5.

Article significance. This study introduces an unconventional class of boundary-value problems in which lateral contraction remains unconstrained, leading to wrinkling instabilities despite the stress fields being less inhomogeneous than those typically observed under classical clamped-edge conditions. Novel evolutions in wrinkling patterns are revealed, including the formation of a second set of wrinkles close to the two opposite obtuse-angled corners of the membrane after the stabilization of the initial central wrinkling. Another possible evolution involves the separation of the central wrinkles and their subsequent migration toward the two opposite corners. These numerical findings are further supported by a closed-form analytical expression that predicts the critical elongation strain leading to central wrinkling, along with the corresponding wrinkling pattern. This research paves the way for designing and tuning the critical conditions and modes of wrinkling, offering valuable insights into how these instabilities can be controlled. It opens up new opportunities for applications across a wide range of fields, from enhancing the performance of lightweight structures to advancing wearable electronic devices.

2. Formulation

2.1. Mechanical model

The equilibrium equations governing the large strains of a hyperelastic membrane are derived by following the geometrically extended version of the Föppl-von Kármán model (eFvK) (Friesecke et al., 2006; Fu et al., 2019; Healey et al., 2013). The unloaded state of the membrane is assumed as initially flat and with a geometry described by a prism of domain volume $\mathbb{V}$ with thickness t and a (flat) base domain $\mathbb{B}_{\mathbf{x}}$, of area A and for which $t \ll \sqrt{A}$ due to the thin membrane assumption. Describing the undeformed position $\mathbf{x}$ in a three-dimensional Cartesian reference system through its coordinates x_1–x_2–z, the undeformed membrane volume $\mathbb{V}$ is given by

$$\mathbb{V} := \left\{ \mathbf{x} \,\middle|\, \{x_1, x_2\} \in \mathbb{B}_{\mathbf{x}}, z \in [-1, 1]\frac{t}{2} \right\}. \tag{1}$$

The deformation function $\mathbf{f}(\mathbf{x}) = \mathbf{x} + \mathbf{u}(x_1, x_2, z)$, mapping the reference configuration $\mathbf{x}$ into the current one, is considered to be described by a displacement vector $\mathbf{u}$ following the Kirchhoff hypothesis, for which the surface normal to the mid-plane remains normal during deformation,

$$\mathbf{u}(x_1, x_2, z) = \begin{Bmatrix} u_1(x_1, x_2, z) \\ u_2(x_1, x_2, z) \\ w(x_1, x_2) \end{Bmatrix} = \begin{Bmatrix} \widetilde{u}_1(x_1, x_2) \\ \widetilde{u}_2(x_1, x_2) \\ w(x_1, x_2) \end{Bmatrix} - z \begin{Bmatrix} w_{,1}(x_1, x_2) \\ w_{,2}(x_1, x_2) \\ 0 \end{Bmatrix}, \tag{2}$$

where (the subscript $,\gamma$ represents the partial derivative $\partial/\partial x_\gamma$ and) $\widetilde{u}_\gamma(x_1, x_2)$ and $w(x_1, x_2)$ are the primary kinematic fields, respectively representative of the in-plane and the out-of-plane displacement components of the mid-plane surface along x_γ ($\gamma = 1, 2$)

and along z. By introducing the gradient operator $\nabla = \{\partial/\partial x_1, \partial/\partial x_2, \partial/\partial z\}$ and the deformation gradient $\mathbf{F} = \nabla\mathbf{f} = \mathbf{I} + \nabla\mathbf{u}$, the (symmetric) Green-Lagrange strain tensor $\mathbf{E} = \left(\mathbf{F}^T\mathbf{F} - \mathbf{I}\right)/2$ evaluated by considering the displacement vector $\mathbf{u}$ (2) finds the following decomposition

$$\mathbf{E}(x_1, x_2, z) = \mathbf{E}^{[p]}(x_1, x_2) + z\,\mathbf{E}^{[\chi]}(x_1, x_2) - \frac{z^2}{4}\mathbf{E}^{[q]}(x_1, x_2), \tag{3}$$

where the tensors $\mathbf{E}^{[p]}$, $\mathbf{E}^{[\chi]}$, and $\mathbf{E}^{[q]}$ (whose components are reported in Appendix A.1) are respectively representative of the constant, linear, and quadratic deformation contributions through the out-of-plane variable z. Considering this decomposition and a hyperelastic response, the (volume) strain energy density ψ can be integrated through the membrane thickness t to achieve the surface strain energy density Ψ as a function of $\mathbf{E}^{[p]}$, $\mathbf{E}^{[\chi]}$, and $\mathbf{E}^{[q]}$

$$\Psi = \int_{-\frac{t}{2}}^{\frac{t}{2}} \psi(\mathbf{E})\mathrm{d}z = \Psi\left(\mathbf{E}^{[p]}, \mathbf{E}^{[\chi]}, \mathbf{E}^{[q]}\right). \tag{4}$$

By assuming an out-of-plane displacement w with small first- and second-surface gradients ($\left\{|\nabla_s w|, t|\nabla_s^2 w|\right\} \ll 1$, where $\nabla_s = \{\partial/\partial x_1, \partial/\partial x_2\}$ is the surface gradient operator), the surface strain energy density Ψ (4) can be approximated according to the extended Föppl-von Kármán theory as the sum of membrane $\Psi^{[m]}\left(\mathbf{E}^{[m]}\right)$ and bending $\Psi^{[b]}\left(\mathbf{E}^{[m]}, \boldsymbol{\kappa}\right)$ energy contributions as (Steigmann, 2013; Wang et al., 2019)

$$\Psi \approx \Psi\left(\mathbf{E}^{[m]}, \boldsymbol{\kappa}\right) = \underbrace{t\,\psi^{[m]}\left(\mathbf{E}^{[m]}\right)}_{\Psi^{[m]}\left(\mathbf{E}^{[m]}\right)} + \underbrace{\frac{t^3}{24}\boldsymbol{\kappa} \cdot \left.\frac{\partial^2\psi^{[m]}\left(\mathbf{E}^{[m]}\right)}{\partial\mathbf{E}^{[m]}\partial\mathbf{E}^{[m]}}\right|_{\mathbf{E}^{[m]}} \boldsymbol{\kappa}}_{\Psi^{[b]}\left(\mathbf{E}^{[m]}, \boldsymbol{\kappa}\right)}, \tag{5}$$

where $\mathbf{E}^{[m]}$ and $\boldsymbol{\kappa}$ are respectively the (symmetric) membrane Green-Lagrange strain and curvature (or bending strain) tensors, defined as the surface components of $\mathbf{E}^{[p]}$ and $\mathbf{E}^{[\chi]}$

$$\begin{aligned}
\mathbf{E}^{[m]} &= \begin{bmatrix} E_{11}^{[p]} & E_{12}^{[p]} \\ E_{12}^{[p]} & E_{22}^{[p]} \end{bmatrix} = \begin{bmatrix} \widetilde{u}_{1,1} + \dfrac{\left(\widetilde{u}_{1,1}\right)^2 + \left(\widetilde{u}_{1,2}\right)^2 + \left(w_{,1}\right)^2}{2} & \dfrac{\widetilde{u}_{1,2} + \widetilde{u}_{2,1} + \widetilde{u}_{1,1}\widetilde{u}_{2,1} + \widetilde{u}_{1,2}\widetilde{u}_{2,2} + w_{,1}w_{,2}}{2} \\ \dfrac{\widetilde{u}_{1,2} + \widetilde{u}_{2,1} + \widetilde{u}_{1,1}\widetilde{u}_{2,1} + \widetilde{u}_{1,2}\widetilde{u}_{2,2} + w_{,1}w_{,2}}{2} & \widetilde{u}_{2,2} + \dfrac{\left(\widetilde{u}_{2,1}\right)^2 + \left(\widetilde{u}_{2,2}\right)^2 + \left(w_{,2}\right)^2}{2} \end{bmatrix}, \\
\boldsymbol{\kappa} &= \begin{bmatrix} E_{11}^{[\chi]} & E_{12}^{[\chi]} \\ E_{12}^{[\chi]} & E_{22}^{[\chi]} \end{bmatrix} = -\begin{bmatrix} w_{,11} & w_{,12} \\ w_{,12} & w_{,22} \end{bmatrix},
\end{aligned} \tag{6}$$

while $\psi^{[m]}$ is the reduced (volume) strain energy density evaluated through variational dimensional reduction by the partial minimization over the out-of-plane strain components,

$$\psi^{[m]}\left(\mathbf{E}^{[m]}\right) = \min_{\left\{E_{13}^{[p]}, E_{23}^{[p]}, E_{33}^{[p]}\right\}} \psi\left(\left[\begin{array}{ccc|c} & \mathbf{E}^{[m]} & & E_{13}^{[p]} \\ & & & E_{23}^{[p]} \\ \hline E_{13}^{[p]} & E_{23}^{[p]} & & E_{33}^{[p]} \end{array}\right]\right). \tag{7}$$

Considering the second Piola-Kirchhoff stress, $\mathbf{S} = \partial\psi(\mathbf{E})/\partial\mathbf{E}$, the partial minimization (7) is mechanically equivalent to solving the through-thickness equilibrium that enforces plane stress conditions (Hilgers and Pipkin, 1992, 1996), which is expressed by

$$S_{j3} = \frac{\partial\psi(\mathbf{E})}{\partial E_{j3}} = 0, \qquad j = 1, 2, 3. \tag{8}$$

The constitutive relations for the membrane force $\mathbf{N}$ and bending moment $\mathbf{M}$ (symmetric) tensors per unit undeformed length[1] follow from the surface strain energy density $\boldsymbol{\Psi}$ (5), obtained under the extended Föppl-von Kármán approximation, as

$$\mathbf{N} = \frac{\partial\Psi\left(\mathbf{E}^{[m]}, \boldsymbol{\kappa}\right)}{\partial\mathbf{E}^{[m]}}, \qquad \mathbf{M} = \frac{\partial\Psi\left(\mathbf{E}^{[m]}, \boldsymbol{\kappa}\right)}{\partial\boldsymbol{\kappa}}, \tag{9}$$

which, by considering the membrane and bending contributions (5), reduce to a nonlinear relation for the membrane force $\mathbf{N}$ in the membrane Green-Lagrange strain $\mathbf{E}^{[m]}$ and a linear relation for the bending moment $\mathbf{M}$ in the curvature tensor $\boldsymbol{\kappa}$ (with stiffness possibly depending nonlinearly on the membrane Green-Lagrange strain $\mathbf{E}^{[m]}$)

$$\mathbf{N}\left(\mathbf{E}^{[m]}\right) = t\frac{\partial\psi^{[m]}\left(\mathbf{E}^{[m]}\right)}{\partial\mathbf{E}^{[m]}}, \qquad \mathbf{M}\left(\mathbf{E}^{[m]}, \boldsymbol{\kappa}\right) = \frac{t^3}{12}\frac{\partial^2\psi^{[m]}\left(\mathbf{E}^{[m]}\right)}{\partial\mathbf{E}^{[m]}\partial\mathbf{E}^{[m]}}\boldsymbol{\kappa}, \tag{10}$$

[1] It is noted that the resultant membrane force $\mathbf{N}$ and bending moment $\mathbf{M}$ are associated with an undeformed unit length as these are evaluated through an integration of the second Piola-Kirchhoff stress distributions across the membrane thickness.

where quadratic terms in the curvature $\boldsymbol{\kappa}$ are neglected in the expression for the membrane force $\mathbf{N}$ $(10)_1$ since $t\,|\nabla_s^2 w| \ll 1$.

By introducing the 2D (membrane) identity tensor $\mathbf{I}_s$ and the outward unit-normal $\mathbf{n}$ and the unit tangent $\mathbf{t}$ vectors along $\partial\mathbb{B}_{\mathbf{x}}$, the equilibrium of the extended Föppl-von Kármán membrane is governed by the indefinite equations (derivation details are deferred to Appendix A.2)

$$\begin{cases} \nabla_s \cdot \left(\nabla_s \cdot \mathbf{M} + \mathbf{N}\nabla_s w\right) = 0, \\ \nabla_s \cdot \left[\left(\mathbf{I}_s + \nabla_s \widetilde{\mathbf{u}}\right)\mathbf{N}\right] = \mathbf{0}. \end{cases} \qquad \text{for } x_1, x_2 \in \mathbb{B}_{\mathbf{x}}, \tag{11}$$

These are complemented by the dual set of stress-free and kinematic boundary conditions on the boundary $\partial\mathbb{B}_{\mathbf{x}}$ of the (flat) surface $\mathbb{B}_{\mathbf{x}}$,

$$\begin{cases} \mathbf{n}\cdot\mathbf{M}\mathbf{n} = 0, & \text{or} \quad \left(\nabla_s w\right)\cdot\mathbf{n} = \overline{w}_{,n}, \\ \left[\mathbf{N}\nabla_s w + \nabla_s\cdot\mathbf{M} + \mathbf{t}\cdot\left(\nabla_s(\mathbf{M}\mathbf{t})\right)\right]\cdot\mathbf{n} = 0, & \text{or} \quad w = \overline{w}, \qquad \text{for } x_1, x_2 \in \partial\mathbb{B}_{\mathbf{x}}, \\ \left(\mathbf{I}_s + \nabla_s\widetilde{\mathbf{u}}\right)\mathbf{N}\mathbf{n} = \mathbf{0}, & \text{or} \quad \widetilde{\mathbf{u}} = \overline{\mathbf{u}}, \end{cases} \tag{12}$$

and the dual set of stress-free and kinematic boundary condition at the possible corner point Γ_j along $\partial\mathbb{B}_{\mathbf{x}}$ $(j = 1, \dots, Q)$

$$[\![\mathbf{n}\cdot\mathbf{M}\mathbf{t}]\!]\big|_{\Gamma_j} = 0, \quad \text{or} \quad w\big|_{\Gamma_j} = \overline{w}, \qquad j = 1, \dots, Q, \tag{13}$$

where (the symbol $[\![\cdot]\!]$ stands for the jump value of the relevant argument at the specific corner point, and) $\overline{\mathbf{u}}$, $\overline{w}$, and $\overline{w}_{,n}$ are the imposed in-plane displacement, out-of-plane displacement and its normal derivative, respectively.

2.2. Hyperelastic constitutive models

Compressible Neo-Hookean (NH) model. The strain energy density ψ_{NH} associated to the compressible Neo–Hookean (NH) material is defined as (Kossa et al., 2023)

$$\psi_{\text{NH}}(\mathbf{E}) = \frac{1}{2}\left\{\mu\left[\frac{\text{tr}\,(\mathbf{I}+2\mathbf{E})}{\sqrt[3]{\det\,(\mathbf{I}+2\mathbf{E})}} - 3\right] + K\left[\sqrt{\det\,(\mathbf{I}+2\mathbf{E})} - 1\right]^2\right\}, \tag{14}$$

where μ and K are the ground-state shear and bulk moduli, the latter connected to the ground Lamé constant λ through $K = \lambda + 2\mu/3$. As the partial minimization (8) performed on the strain energy density $\psi_{\text{NH}}(\mathbf{E})$ (14) leads to a set of nonlinear equations for the out-of-plane strains $E^{[p]}_{i3}\left(\mathbf{E}^{[m]}\right)$ $(i = 1, 2, 3)$, the reduced strain energy density $\psi^{[m]}_{\text{NH}}\left(\mathbf{E}^{[m]}\right)$ cannot be expressed in a closed form and must be evaluated numerically. Then, nonlinear relations for the membrane force $\mathbf{N}^{\text{NH}}\left(\mathbf{E}^{[m]}\right)$ and bending moment $\mathbf{M}^{\text{NH}}\left(\mathbf{E}^{[m]}, \boldsymbol{\kappa}\right)$ follows through the constitutive relation (10), the latter with a bending stiffness varying with the membrane strain $\mathbf{E}^{[m]}$ (except in the small-strain limit).

Saint Venant–Kirchhoff (SVK) model. The strain energy density ψ_{SVK} is given for the Saint Venant–Kirchhoff (SVK) material by (Timoshenko and Woinowsky-Krieger, 1959)

$$\psi_{\text{SVK}}(\mathbf{E}) = \frac{1}{2}\left\{\lambda[\text{tr}(\mathbf{E})]^2 + 2\mu\,\text{tr}\left(\mathbf{E}^2\right)\right\}. \tag{15}$$

Being the strain energy $\psi_{\text{SVK}}(\mathbf{E})$ (15) a quadratic form in the Green-Lagrange strain $\mathbf{E}$, the partial minimization (8) leads to a set of linear equations whose solution is given by the following out-of-plane strain components

$$E_{13} = E_{23} = 0, \qquad E_{33} = -\frac{\lambda(E_{11} + E_{22})}{\lambda + \mu}, \tag{16}$$

and therefore the reduced strain energy density $\psi^{[m]}_{\text{SVK}}\left(\mathbf{E}^{[m]}\right)$ follows as

$$\psi^{[m]}_{\text{SVK}}\left(\mathbf{E}^{[m]}\right) = \frac{1}{2}\left\{\lambda_{ps}\left[\text{tr}\left(\mathbf{E}^{[m]}\right)\right]^2 + 2\mu\,\text{tr}\left(\left(\mathbf{E}^{[m]}\right)^2\right)\right\}, \tag{17}$$

where λ_{ps} is the Lamé constant under plane stress conditions, $\lambda_{ps} = 2\lambda\mu/(\lambda + 2\mu)$. By considering the relation connecting the Lamé constants λ and μ to the Young's modulus E and Poisson's ratio ν, and by introducing the membrane bending stiffness D,

$$\lambda = \frac{E\,\nu}{(1+\nu)(1-2\nu)}, \qquad \mu = \frac{E}{2(1+\nu)}, \qquad D = \frac{E\,t^3}{12(1-\nu^2)}, \tag{18}$$

the membrane force $\mathbf{N}^{\text{SVK}}$ and bending moment $\mathbf{M}^{\text{SVK}}$ reduce to linear functions of the membrane Green-Lagrange strain $\mathbf{E}^{[m]}$ and of the curvature $\boldsymbol{\kappa}$ (with constant bending stiffness D), respectively,

$$\mathbf{N}^{\text{SVK}}\left(\mathbf{E}^{[m]}\right) = \frac{E\,t}{1-\nu^2}\left[\nu\,\text{tr}\left(\mathbf{E}^{[m]}\right)\mathbf{I}_s + (1-\nu)\,\mathbf{E}^{[m]}\right], \qquad \mathbf{M}^{\text{SVK}}(\boldsymbol{\kappa}) = D\left[\nu\,\text{tr}\left(\boldsymbol{\kappa}\right)\mathbf{I}_s + (1-\nu)\,\boldsymbol{\kappa}\right]. \tag{19}$$

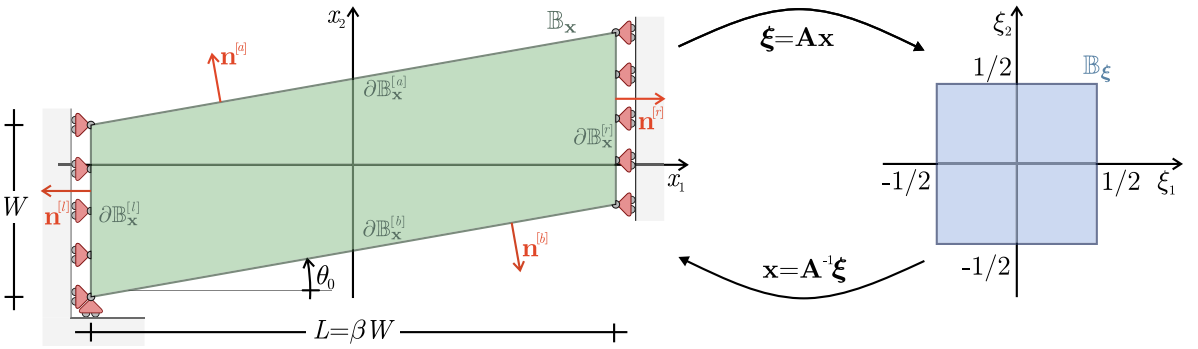

Fig. 3. (Left) Undeformed parallelogram geometry of the hyperelastic membrane and boundary conditions. (Right) Reparameterization of the physical parallelogram domain $\mathbb{B}_x$ on the auxiliary unit square domain $\mathbb{B}_\xi$ through the transformation matrix $\mathbf{A}$ (32).

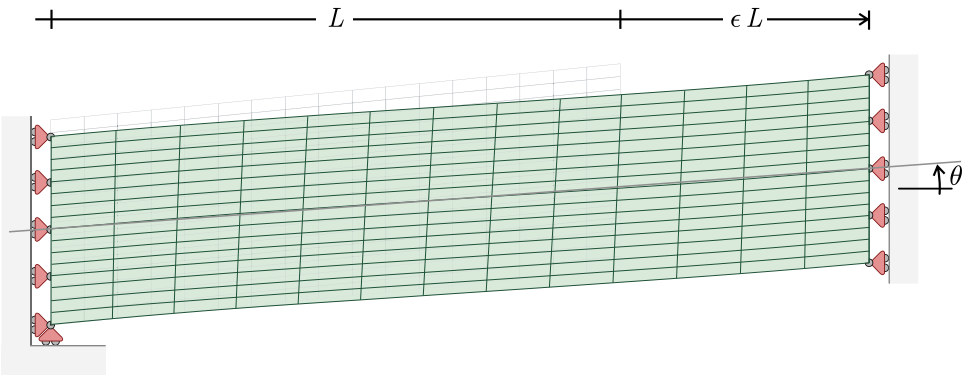

Fig. 4. Undeformed (gray) and deformed (green) planar configurations for the considered parallelogram-shaped membrane, the latter under boundary conditions $(27)_3$, (28), and (29) described by an elongation strain ϵ. A deformed mesh is reported as a result from Finite Element simulation (Section 3) for $\epsilon = 44\,\%$. The current inclination angle θ corresponding to Eq. (37) is also shown as a measure of the (average) inclination of the stress-free edges.

Linear elastic (LE) model. When the displacement gradient is sufficiently small ($|\nabla\mathbf{u}| \ll 1$), the higher-order (nonlinear) terms become negligible. It follows that the Green–Lagrange strain $\mathbf{E}$ and its membrane counterpart $\mathbf{E}^{[m]}$ reduce to the corresponding linearized strain tensors $\boldsymbol{\epsilon}$ and $\boldsymbol{\epsilon}^{[m]}$, namely $\mathbf{E} = \boldsymbol{\epsilon} = \left[\nabla\mathbf{u} + (\nabla\mathbf{u})^T\right]/2$ and $\mathbf{E}^{[m]} = \boldsymbol{\epsilon}^{[m]} = \left[\nabla_s\widetilde{\mathbf{u}} + (\nabla_s\widetilde{\mathbf{u}})^T\right]/2$, and therefore

$$\epsilon_{11}^{[m]} = \widetilde{u}_{1,1}, \quad \epsilon_{12}^{[m]} = \frac{\widetilde{u}_{1,2} + \widetilde{u}_{2,1}}{2}, \quad \epsilon_{22}^{[m]} = \widetilde{u}_{2,2}. \tag{20}$$

In this circumstance, both the compressible Neo-Hookean (14) and Saint Venant–Kirchhoff (17) models reduce to the linear elastic (LE) model by providing the celebrated linear elastic expressions of the Föppl-von Kármán plate (Calladine, 1983; Timoshenko and Woinowsky-Krieger, 1959) for the membrane force $\mathbf{N}^{\mathrm{LE}}$ and bending moment $\mathbf{M}^{\mathrm{LE}}$

$$\mathbf{N}^{\mathrm{LE}}\left(\boldsymbol{\epsilon}^{[m]}\right) = \frac{E\,t}{1-\nu^2}\left[\nu\ \mathrm{tr}\left(\boldsymbol{\epsilon}^{[m]}\right)\mathbf{I}_s + (1-\nu)\,\boldsymbol{\epsilon}^{[m]}\right], \qquad \mathbf{M}^{\mathrm{LE}}(\boldsymbol{\kappa}) = D\left[\nu\ \mathrm{tr}\left(\boldsymbol{\kappa}\right)\mathbf{I}_s + (1-\nu)\,\boldsymbol{\kappa}\right]. \tag{21}$$

2.3. Geometry and boundary conditions

In contrast to the rectangular and circular geometries with edge contraction prevented along portions of their boundaries, which are usually considered to investigate wrinkling, a parallelogram-shaped membrane that is free to contract laterally is considered here, Fig. 3 (left).

Differently from the conventional setups, this 'unconventional' configuration allows refined tuning of the inhomogeneity level through the obliquity angle $(\pi/2 - \theta_0)$ of the parallelogram. In particular, it leads to less inhomogeneous mechanical fields during membrane elongation, as it avoids the strong edge-decay effect typically associated with constrained lateral contraction. Moreover, the mechanical fields smoothly converge to the homogeneous solution in the right-angle limit ($\theta_0 = 0$), where the configuration reduces to a rectangular membrane under uniform tension. The low level of inhomogeneity can be appreciated from Fig. 4, where the deformed configuration for an elongation strain $\epsilon = 44\,\%$ is reported as result of a planar Finite Element simulation (Section 3).

The undeformed base domain $\mathbb{B}_{\mathbf{x}}$ of parallelogram shape is considered to have two sides parallel to the x_2-axis, while the other two are inclined with respect to the x_1-axis by the initial (undeformed) inclination angle θ_0 (Fig. 3, left),

$$\mathbb{B}_{\mathbf{x}} := \left\{ \mathbf{x} \,\middle|\, -\frac{L}{2} \le x_1 \le \frac{L}{2},\ -\frac{W}{2} + x_1 \tan\theta_0 \le x_2 \le \frac{W}{2} + x_1 \tan\theta_0 \right\}, \tag{22}$$

where L and W denote the undeformed length and width of the original parallelogram flat membrane.

For the following analysis, it is instrumental to introduce two dimensionless parameters defining the width-to-thickness ratio α and the (in-plane) aspect ratio β as

$$\alpha = \frac{W}{t} \gg 1, \qquad \beta = \frac{L}{W}. \tag{23}$$

The boundary $\partial\mathbb{B}_{\mathbf{x}}$ of the domain $\mathbb{B}_{\mathbf{x}}$ can be described as the union of four portion boundaries $\partial\mathbb{B}_{\mathbf{x}}^{[a]}$, $\partial\mathbb{B}_{\mathbf{x}}^{[b]}$, $\partial\mathbb{B}_{\mathbf{x}}^{[l]}$, and $\partial\mathbb{B}_{\mathbf{x}}^{[r]}$ defined as

$$\left.\begin{matrix}\partial\mathbb{B}_{\mathbf{x}}^{[a]} \\ \partial\mathbb{B}_{\mathbf{x}}^{[b]}\end{matrix}\right\} := \left\{ \mathbf{x} \,\middle|\, -\frac{L}{2} \le x_1 \le \frac{L}{2}, x_2 = \pm\frac{W}{2} + x_1 \tan\theta_0 \right\}, \qquad \left.\begin{matrix}\partial\mathbb{B}_{\mathbf{x}}^{[l]} \\ \partial\mathbb{B}_{\mathbf{x}}^{[r]}\end{matrix}\right\} := \left\{ \mathbf{x} \,\middle|\, x_1 = \mp\frac{L}{2}, -\frac{W \pm L\tan\theta_0}{2} \le x_2 \le \frac{W \mp L\tan\theta_0}{2} \right\}, \tag{24}$$

associated with the following corresponding outward unit normal vectors

$$\mathbf{n}^{[a]} = -\mathbf{n}^{[b]} = \begin{Bmatrix} -\sin\theta_0 \\ \cos\theta_0 \end{Bmatrix}, \qquad \mathbf{n}^{[r]} = -\mathbf{n}^{[l]} = \begin{Bmatrix} 1 \\ 0 \end{Bmatrix}. \tag{25}$$

The hyperelastic parallelogram is subject to different boundary conditions along the different portion of its boundary (Fig. 3, left). These correspond to traction-free boundary condition along $\mathbb{B}_{\mathbf{x}}^{[a]}$ and $\mathbb{B}_{\mathbf{x}}^{[b]}$,

$$\begin{cases} \mathbf{n}\cdot\mathbf{M}\mathbf{n} = 0, \\ \left[\mathbf{N}\nabla_s w + \nabla_s\cdot\mathbf{M} + \mathbf{t}\cdot\left(\nabla_s(\mathbf{M}\mathbf{t})\right)\right]\cdot\mathbf{n} = 0, \\ \left(\mathbf{I}_s + \nabla_s\widetilde{\mathbf{u}}\right)\mathbf{N}\mathbf{n} = \mathbf{0}, \end{cases} \qquad \text{for } x_1, x_2 \in \partial\mathbb{B}_{\mathbf{x}}^{[a]} \cup \mathbb{B}_{\mathbf{x}}^{[b]}, \tag{26}$$

and to the presence of tangential rollers along $\partial\mathbb{B}_{\mathbf{x}}^{[l]}$ and $\partial\mathbb{B}_{\mathbf{x}}^{[r]}$, namely

$$\begin{cases} \mathbf{e}_1\cdot\mathbf{M}\mathbf{e}_1 = 0, \\ w = 0, \\ \left[\left(\mathbf{I}_s + \nabla_s\widetilde{\mathbf{u}}\right)\mathbf{N}\mathbf{e}_1\right]\cdot\mathbf{e}_2 = 0, \end{cases} \qquad \text{for } x_1, x_2 \in \partial\mathbb{B}_{\mathbf{x}}^{[l]} \cup \mathbb{B}_{\mathbf{x}}^{[r]}, \tag{27}$$

where $\mathbf{e}_1$ and $\mathbf{e}_2$ are the unit vectors respectively parallel to the x_1 and x_2 axis, and complemented by the following prescribed displacement along x_1

$$\widetilde{u}_1 = 0, \qquad \text{for } x_1, x_2 \in \partial\mathbb{B}_{\mathbf{x}}^{[l]}, \qquad \text{and} \qquad \widetilde{u}_1 = \epsilon L, \qquad \text{for } x_1, x_2 \in \partial\mathbb{B}_{\mathbf{x}}^{[r]}, \tag{28}$$

where ϵ is the imposed elongation strain, $\epsilon > 0$. In order to avoid the possibility for rigid-body motions along x_2, a corresponding null displacement component is considered for the acute-angled corner with negative coordinates,

$$\widetilde{u}_2 = 0, \qquad \text{for } x_1, x_2 \in \Gamma_{lb} \equiv \partial\mathbb{B}_{\mathbf{x}}^{[l]} \cap \partial\mathbb{B}_{\mathbf{x}}^{[b]}, \tag{29}$$

The lateral contraction of the parallelogram membrane during stretching is enabled by the presence of tangential rollers placed along the boundaries $\partial\mathbb{B}_{\mathbf{x}}^{[l]}$ and $\partial\mathbb{B}_{\mathbf{x}}^{[r]}$, as prescribed by the boundary condition $(27)_3$. This boundary condition can be experimentally realized by exploiting the Saint-Venant fixture presented in Misseroni et al. (2022). In standard wrinkling analyses, the rollers are replaced by clamps to inhibit lateral contraction, and the governing equations therefore differ from the set (26)–(29) only in the substitution of boundary condition $(27)_3$ with $\widetilde{\mathbf{u}}\cdot\mathbf{t} = 0$.

Section 3 demonstrates the rich and diverse spectrum of wrinkling patterns produced in this mechanical problem.

2.4. Reparameterization of the parallelogram domain $\mathbb{B}_{\mathbf{x}}$ onto the unit square $\mathbb{B}_{\boldsymbol{\xi}}$

Introducing the auxiliary (normalized) coordinates ξ_1 and ξ_2, the parallelogram domain $\mathbb{B}_{\mathbf{x}}$ can be transformed through the uniform linear transformation

$$\boldsymbol{\xi} = \mathbf{A}(\beta, \theta_0)\,\mathbf{x}, \tag{30}$$

onto a unit square domain $\mathbb{B}_{\boldsymbol{\xi}}$ (and vice versa), defined as (Fig. 3, right)

$$\mathbb{B}_{\xi} := \left\{ \boldsymbol{\xi} \,\middle|\, -\frac{1}{2} < \xi_1 < \frac{1}{2},\ -\frac{1}{2} < \xi_2 < \frac{1}{2} \right\}. \tag{31}$$

The linear uniform transformation is described by the (non-singular) transformation matrix $\mathbf{A}(\beta, \theta_0)$ given by

$$\mathbf{A}(\beta, \theta_0) = \frac{1}{W}\begin{bmatrix} \dfrac{1}{\beta} & 0 \\ -\tan\theta_0 & 1 \end{bmatrix}. \tag{32}$$

The introduction of the auxiliary coordinates ξ_1 and ξ_2 is instrumental in the following analysis to either simplify the identification of points within the parallelogram domain and performing the perturbation approach to achieve an approximated equation ruling the critical elongation strain ϵ_{cr} for the realization of central wrinkling.

3. Wrinkling, self-restabilization, and re-wrinkling from numerical simulations

The evolution of the hyperelastic parallelogram-shaped membrane is investigated under the monotonic increase of the elongation strain ϵ to uncover the potential bifurcation (critical) conditions from the trivial path. These conditions are found to provide to the membrane a smooth transition from a fully planar state to a non-planar state (or vice versa), associated with the appearance, disappearance, and reappearance of wrinkles, and the corresponding post-critical response. Due to the complexity of analytically solving the non-linear differential problem (11), (26)–(29) governing the equilibrium of hyperelastic parallelogram-shaped membranes, the Finite Element (FE) method is employed (Section 3.1). The investigation reveals a diverse spectrum of mechanical responses, with the membrane potential to restabilize wrinkling and subsequently rewrinkle in a different location (Section 3.2). To provide motivation for this novel response, an in-depth analysis of the in-plane fields is further conducted (Section 3.3).

3.1. Finite element solver and numerical simulation details

Finite Element (FE) simulations are performed with the commercial software Abaqus 2023, where the NH and SVK constitutive models (Section 2.2) are both available. A comparison in the mechanical response between these two material models (reported for completeness in Appendix B) shows qualitative similarities, according to Wong and Pellegrino (2006b) for a different setup. Therefore, for conciseness, the results are presented with reference only to the NH model (14). The selected parameters for the NH membrane are Young's modulus $E = 200$ MPa, Poisson's ratio $\nu = 0.33$, and a width-to-thickness ratio $\alpha = 1500$, unless stated otherwise. Analyses are mainly performed with varying two geometric parameters defining the undeformed planar parallelogram shape, the initial inclination angle $\theta_0 \in [0, 6°]$ and the aspect ratio $\beta \in [2, 5]$. Due to the tangential roller constraints as edge boundary conditions (instead of the usually investigated clamps) along $\partial\mathbb{B}_{\mathbf{x}}^{[l]}$ and $\partial\mathbb{B}_{\mathbf{x}}^{[r]}$, the limit case of undeformed rectangular membrane ($\theta_0 = 0$) homogeneously deforms into another rectangle with increasing ϵ, where wrinkling never occurs because a uniform tension parallel to the x_1 axis is present and the compressive state is absent. Differently, by considering a non-null initial inclination angle $\theta_0 \neq 0$, the membrane domain is a parallelogram where an inhomogeneous stress field is realized, introducing some compressive principal component over the domain and possibly leading to wrinkling instability. This is indeed what can be observed, as shown in the following even for quasi-rectangular geometries, namely for small inclination angle values, $|\theta_0| \ll \theta_0^2$.

An essential aspect of the numerical implementation regards the FE discretization and mesh convergence. The simulations employ four-node quadrilateral shell elements (`S4R`) with reduced integration, which are particularly well-suited for thin-shell problems because they accommodate finite membrane strains and large rotations while mitigating common numerical artifacts. To ensure accurate resolution of wrinkling wavelengths and amplitudes, a progressive mesh refinement was conducted. Beyond a certain refinement level, the maximum out-of-plane displacement and stress distributions converged, exhibiting negligible variation with further refinement. Consequently, the final mesh was deemed sufficiently accurate to capture the critical features of the wrinkling response under the applied loads and boundary conditions.

Different numerical solvers are available for analyzing the stability phenomena under investigation. In most cases, the `Riks` (also known as arc-length) method is adopted to trace the equilibrium path after bifurcation. In addition to manage possible snap-through and snap-back behaviours (which are however not displayed in the considered problem), the `Riks` method effectively maintains a robust convergence even amid severe nonlinearities that occur once wrinkling commences. Additionally, `dynamic implicit` simulations and static analyses with the `Stabilize` option are used to validate the `Riks` method results. These methods yield consistent out-of-plane displacement profiles and stress distributions, differing primarily in the computational cost. It is observed that static analysis with the `Stabilize` option showed better performance and numerical stability; therefore, it was selected for all the present analyses. While the `dynamic implicit` and `Riks` methods offer no distinctive advantages over the `Stabilize` approach in this context, the latter proves to be more computationally efficient and numerically stable.

The numerical investigation under all of these approaches requires the introduction of an out-of-plane imperfection in the membrane to trigger the wrinkling instability; without it, the simulation may fail to capture the bifurcation from the trivial (flat state) path. Indeed, numerical round-off errors are typically insufficient to break the inherent problem symmetry and trigger wrinkling in planar membrane under in-plane loading (Wong and Pellegrino, 2006b). To this purpose, the out-of-plane imperfection is considered as an initial non-planar shape, $w^*(x_1, x_2)$, defined as

$$w^*(x_1, x_2) = t \sum_{i=1}^{2} s_i \, \phi_i(x_1, x_2), \tag{33}$$

where the (normalized) shape functions $\phi_i(x_1, x_2)$ $(i = 1, 2)$ can be introduced by following two different approaches, either as random compatible generation or as the first two critical modes of buckling, $\phi_i(x_1, x_2) = \phi_{\mathrm{cr},i}(x_1, x_2)$. Through each of the two approaches a different non-symmetric initial non-planar state is realized, however, both leading to the same critical conditions and post-critical response. When the shape functions $\phi_i(x_1, x_2)$ are defined as the critical modes, these can be found through a classical `Buckling analysis` (under tension) applied to parallelogram membrane under the boundary conditions under considerations.[2] The coefficients s_i $(i = 1, 2)$ define the amplitude applied to respective shape function $\phi_i(x_1, x_2)$, where the resulting imperfection amplitude

[2] It is worth mentioning that, similar to other planar symmetric geometries, the critical modes of parallelogram membranes exhibit either rotational symmetry or skew-symmetry of order 2, with only a minimal difference in the corresponding critical values.

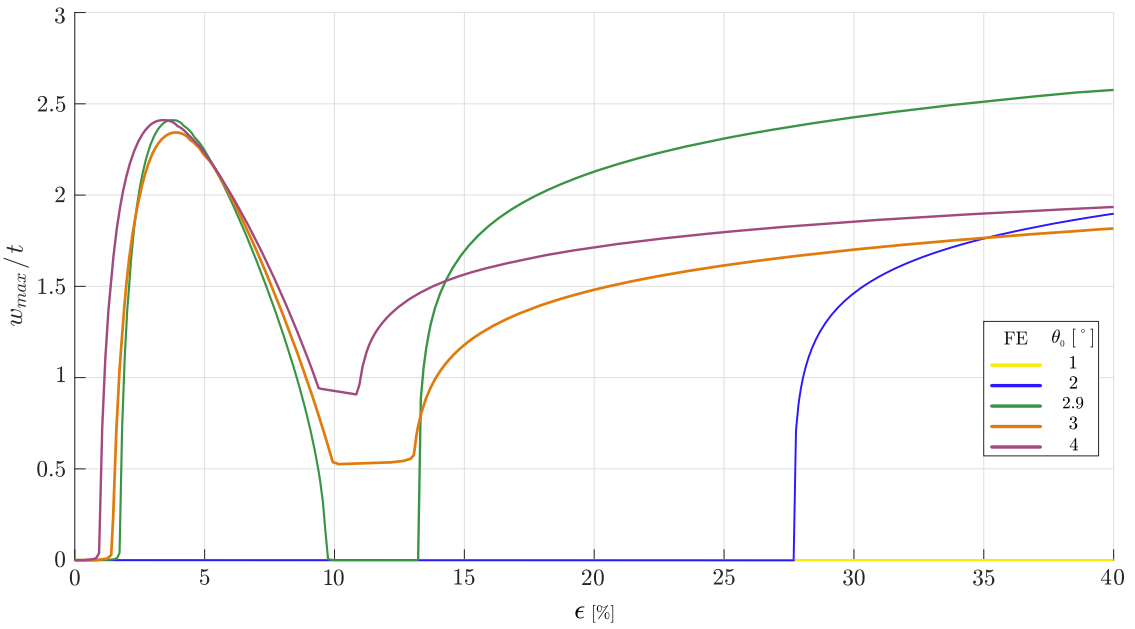

Fig. 5. Maximum value of the out-of-plane displacement $w_{\max}$, normalized through division by the membrane thickness t, as a function of the elongation strain ϵ from FE simulations. Response is reported for five NH membranes with the same width-to-thickness ratio $\alpha = 1500$, (in-plane) aspect ratio $\beta = 3$, and Poisson's ratio $\nu = 0.33$, and differing only in the initial inclination angle $\theta_0 = \{1, 2, 2.9, 3, 4\}°$.

is constrained to provide $\left|w^*(x_1, x_2)/t\right| < 0.02$ for $\theta_0 \in [2, 6]°$ and $\left|w^*(x_1, x_2)/t\right| < 0.1$ for $\theta_0 \in [0, 2]°$ $\forall\, \mathbf{x} \in \mathbb{B}_{\mathbf{x}}$. Maintaining the out-of-plane imperfection at sufficiently small levels is crucial to prevent them from dominating the physical response, while still allowing out-of-plane wrinkling to occur under tensile stress.

3.2. Bifurcations and the four different types of wrinkling pattern evolution

To start our analysis, the elongation test is performed on five compressible Neo-Hookean parallelogram membranes with aspect ratio $\beta = 3$ (and the other parameters as defined in Section 3.1) and differing only in the undeformed inclination angle $\theta_0 = \{1, 2, 2.9, 3, 4\}°$. The corresponding results are first reported in Fig. 5 as the maximum absolute value of the out-of-plane displacement over the membrane domain $w_{\max}$,

$$w_{max} = \max_{\mathbf{x} \in \mathbb{B}_{\mathbf{x}}} \left|w(x_1, x_2)\right|, \tag{34}$$

normalized through division of the membrane thickness t, at increasing elongation strain ϵ.

Although the initial inclination angle θ_0 spans a narrow range of small values, the response exhibits significant variation across the considered cases, with outcomes featuring none, one, or three bifurcations in association with a corresponding number of critical values ϵ_{cr} of the elongation strain. More specifically:

- $\theta_0 = 1°$: No bifurcation is displayed. The membrane always remains under a planar state at increasing elongation strain ϵ;
- $\theta_0 = 2°$: A single bifurcation is displayed only at large strains at the critical elongation strain $\epsilon_{\text{cr}} \simeq 27\,\%$. The maximum wrinkling amplitude monotonically increases under increasing elongation strain $\epsilon > \epsilon_{\text{cr}}$;
- $\theta_0 = 2.9°$: Three bifurcations are detected at the critical elongation strains $\epsilon_{\text{cr}} \simeq \{1.55, 9.5, 13\}\%$. After the first bifurcation at small strain ($\epsilon_{\text{cr}}^{\text{I}} \simeq 1.55\,\%$), the wrinkling amplitude initially increases, but then decreases, ultimately vanishing at the second bifurcation ($\epsilon_{\text{cr}}^{\text{II}} \simeq 9.5\,\%$), corresponding to the self-restabilization of the planar state. After the second bifurcation the planar state is maintained until the third bifurcation is met at large strains ($\epsilon_{\text{cr}}^{\text{III}} \simeq 13\,\%$), which leads to the monotonic increase of the wrinkling amplitude under increasing elongation strain $\epsilon > \epsilon_{\text{cr}}^{\text{III}}$;
- $\theta_0 = 3°$, $4°$: A single bifurcation is displayed at small strains for a respective critical elongation strain $\epsilon_{\text{cr}} \simeq 1.25\,\%$ and $0.8\,\%$. The plane state does not recover the stability although the maximum wrinkling amplitude does not show a monotonically increasing response for any elongation strain ϵ after the (unique) bifurcation, but only for $\epsilon \gtrsim 12.5\,\%$ and $11\,\%$, respectively.

To better understand the differences in the response of the five described cases, the maps of the out-of-plane displacement w are shown in Fig. 1 on the corresponding deformed membrane at four different levels of elongation strain $\epsilon = \{1.5, 7.8, 14, 30\}\%$. This representation offers further insight into the evolution of the wrinkling pattern, which, throughout the entire deformation process, exhibits a long wavelength parallel to the x_1-axis. More specifically, it reveals that, in addition to the common smooth variation in the wrinkling wavelengths, the considered boundary-value problem allows for the possibility of the wrinkling to be displayed at

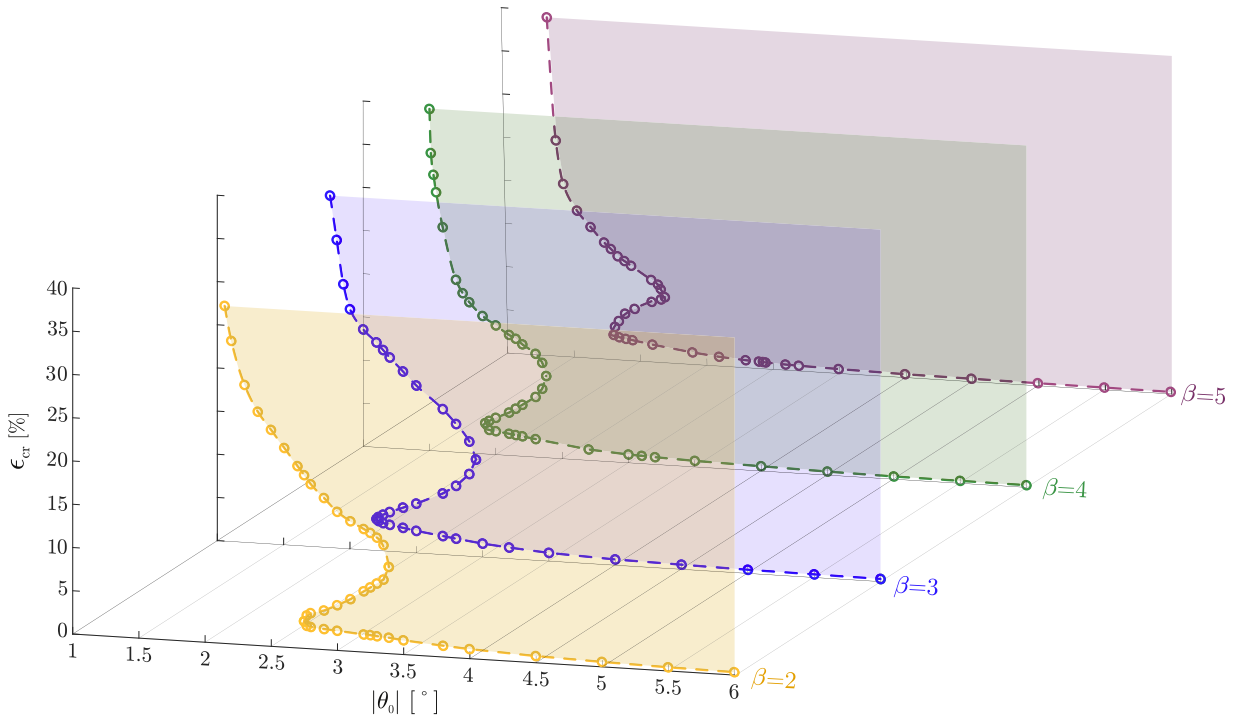

Fig. 6. Critical elongation strains ϵ_{cr} evaluated from FE simulations as functions of the magnitude of the initial inclination angle $|\theta_0|$ and different values of aspect ratio $\beta = \{2, 3, 4, 5\}$ of the parallelogram-shaped membrane. The colored regions represent condition for which a non-planar configuration is displayed. None, one, or three critical values ϵ_{cr} for the elongation strain can be found for given pairs of $|\theta_0|$ and β.

Table 1
Number of bifurcations and the corresponding wrinkling pattern evolution under a monotonic elongation test for the subsets $\mathcal{O}$, $\mathcal{A}_1$, $\mathcal{B}_3$, and $\mathcal{B}_1$.

	Number of bifurcations	Pattern evolution of wrinkle parallel to the x_1-axis
$\mathcal{O}$	0	flat configuration only
$\mathcal{A}_1$	1	flat → obtuse-angled corners wrinkling
$\mathcal{B}_3$	3	flat → central wrinkling → flat → obtuse-angled corners wrinkling
$\mathcal{B}_1$	1	flat → central wrinkling → obtuse-angled corners wrinkling

different locations within the membrane domain. Indeed, for the same initial geometry, the wrinkling may appear over the central region or close to the two obtuse-angled corners, depending on the imposed strain level. The wrinkling evolution between these two locations may occur with ($\theta_0 = 2.9°$) or without ($\theta_0 = 3°$ and 4°) an intermediate restabilization of the flat configuration. Therefore, the central wrinkling totally disappears before the corner ones arise in the former case ($\theta_0 = 2.9°$), while the central wrinkling splits and migrates towards two wrinkling islands close to the two obtuse-angled corners in the latter case ($\theta_0 = 3°$ and 4°). Interestingly, a small variation in the initial inclination angle θ_0, from 2.9° to 3°, leads to a dramatic change in the wrinkling evolution, Figs. 1 and 5.

The critical values ϵ_{cr} of the elongation strain with varying the inclination angle θ_0 are reported in Fig. 6 for different membrane aspect ratio $\beta = \{2, 3, 4, 5\}$.

This result, together with the corresponding wrinkling pattern evolutions (not reported for conciseness), shows that, within the considered ranges of membrane aspect ratio β and initial inclination angle θ_0, the four distinct types of wrinkling pattern evolution are in general possible. These are identified as $\mathcal{O}$, $\mathcal{A}_1$, $\mathcal{B}_3$, and $\mathcal{B}_1$, whose description is summarized in Table 1.

The pairs of membrane parameters β and θ_0 associated to each one of the four types of wrinkling pattern evolution are shown in Fig. 7 through regions of different colors ($\mathcal{O}$ as white, $\mathcal{A}_1$ as orange, $\mathcal{B}_3$ as red, and $\mathcal{B}_1$ as blue).

For completeness, it is worth to mention that a fifth behaviour has also been observed in the simulation of parallelogram-shaped membrane under the elongation process. This fifth behaviour is associated to a first bifurcation displayed through edge wrinkling parallel to the x_2-axis close to the two acute-angled corners has been also found. This response falls outside the $\beta - \theta_0$ domain reported in Fig. 7 and is briefly addressed in Section 3.4, while its thorough analysis is left to future research.

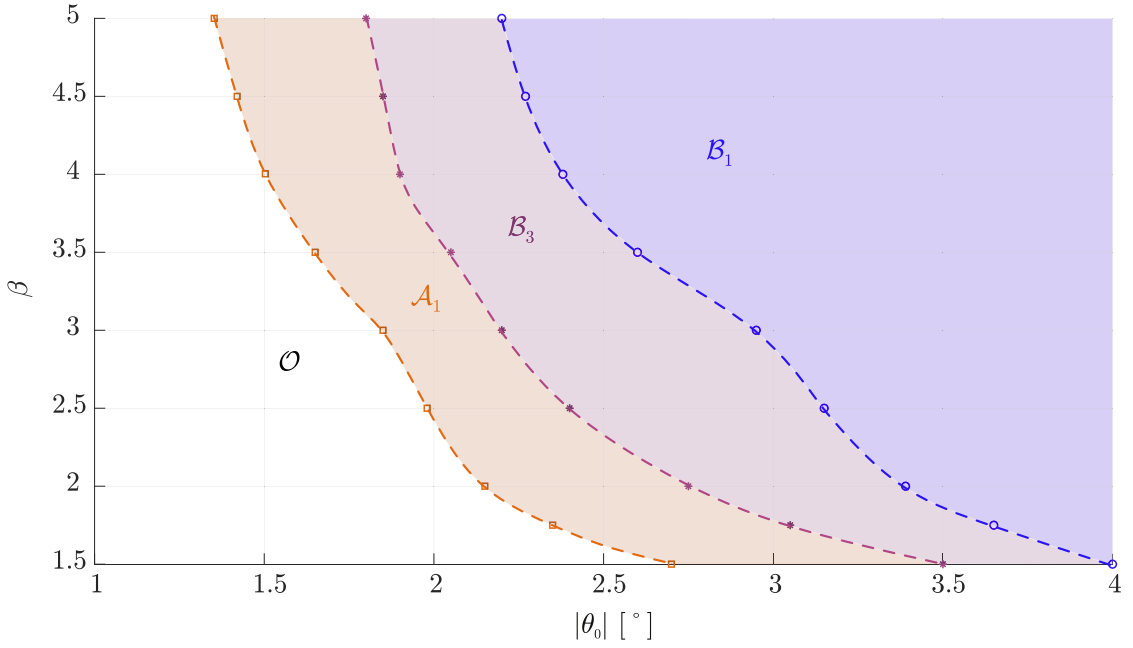

Fig. 7. Wrinkling pattern evolution types $\mathcal{O}$, $\mathcal{A}_1$, $\mathcal{B}_3$, and $\mathcal{B}_1$ (as described in Table 1) identified as regions of the magnitude of the initial inclination angle $|\theta_0|$ and aspect ratio β pairs evaluated from FE simulations.

3.3. In-plane response

The complex interplay between elasticity and geometry defines the broad landscape in the wrinkling pattern evolution. The primary factor contributing to this interplay relies on the large change in the deformed configuration, shown to occur even at limited small strains, leading to the alignment with the x_1-axis of the two inclined free edges during the stretching process. To provide an overview of the nonlinear in-plane response, the results from plane-stress simulations ($w = 0$, no out-of-plane displacement allowed) are examined in terms of the minimum in-plane (compressive) stress component and the inclination angle to show how these change with the increase of the elongation strain ϵ.

3.3.1. Compressive in-plane principal Cauchy stress

The maps of the minimum (compressive) in-plane principal component $\sigma_{min,c}$ of the Cauchy stress $\boldsymbol{\sigma}$ reported in Fig. 8 are associated with the planar state enforced to the membrane geometries and the corresponding elongation levels ϵ considered in Fig. 1. The minimum in-plane principal component $\sigma_{min,c}$ is the compressive (minimum and negative) stress with an inclination ϕ with respect to the x_1-axis defined as

$$\sigma_{min,c} = \min\{0, \sigma_{min}\}, \quad \text{with} \quad \sigma_{min} = \frac{\sigma_{11}+\sigma_{22}}{2} - \sqrt{\left(\frac{\sigma_{11}-\sigma_{22}}{2}\right)^2 + \sigma_{12}^2}, \qquad \phi = \frac{\pi}{2} + \frac{1}{2}\arctan\left(\frac{2\sigma_{12}}{\sigma_{11}-\sigma_{22}}\right), \tag{35}$$

where, under a planar configuration, the Cauchy stress $\boldsymbol{\sigma}$ is uniform across the membrane thickness t and can be evaluated from the membrane force $\mathbf{N}$ $(10)_1$ through

$$\boldsymbol{\sigma} = \frac{\mathbf{F}\mathbf{N}\mathbf{F}^T}{t \det[\mathbf{F}]}. \tag{36}$$

Besides its rotational symmetry of order 2 property, it can be observed that the map becomes increasingly inhomogeneous with the increase of the elongation strain ϵ and for higher values of the initial inclination angle θ_0. Indeed, among the reported cases, the case $\theta_0 = 1°$ is visibly the one with the most limited inhomogeneity in the compression state and for this reason no wrinkling is realized.

Apart from the two compressive edge regions at the two acute-angled corners, the map inhomogeneity can primarily manifest in two locations: in the central region and in the proximity of the two obtuse-angled corners. These two regions are where wrinkles may arise and, interestingly, the highest compressive state is around the central region ($\xi_1 = \xi_2 = 0$) at small strain level, while is close to quadrant centers ($\xi_1 = -\xi_2 = \pm 1/4$) at larger strain. As observed, the transition in the wrinkling location may occur either through the intermediate restabilization of the flat state or via the separation of the wrinkling, followed by its migration toward two wrinkling islands at the two obtuse-angled corners. From Fig. 8, these two different evolutions are respectively shown to be associated with a weaker and stronger compressive state in the central region. To further appreciate this aspect, the compressive in-plane principal stress $\sigma_{min,c}$ at the center ($\xi_1 = \xi_2 = 0$) and at the quadrant centers ($\xi_1 = -\xi_2 = \pm 1/4$) is reported as a function of the elongation strain ϵ in Fig. 9 for the membranes with $\theta_0 = \{2, 2.9, 3, 4\}°$. The different evolutions confirm linearity in θ_0 for the considered small values

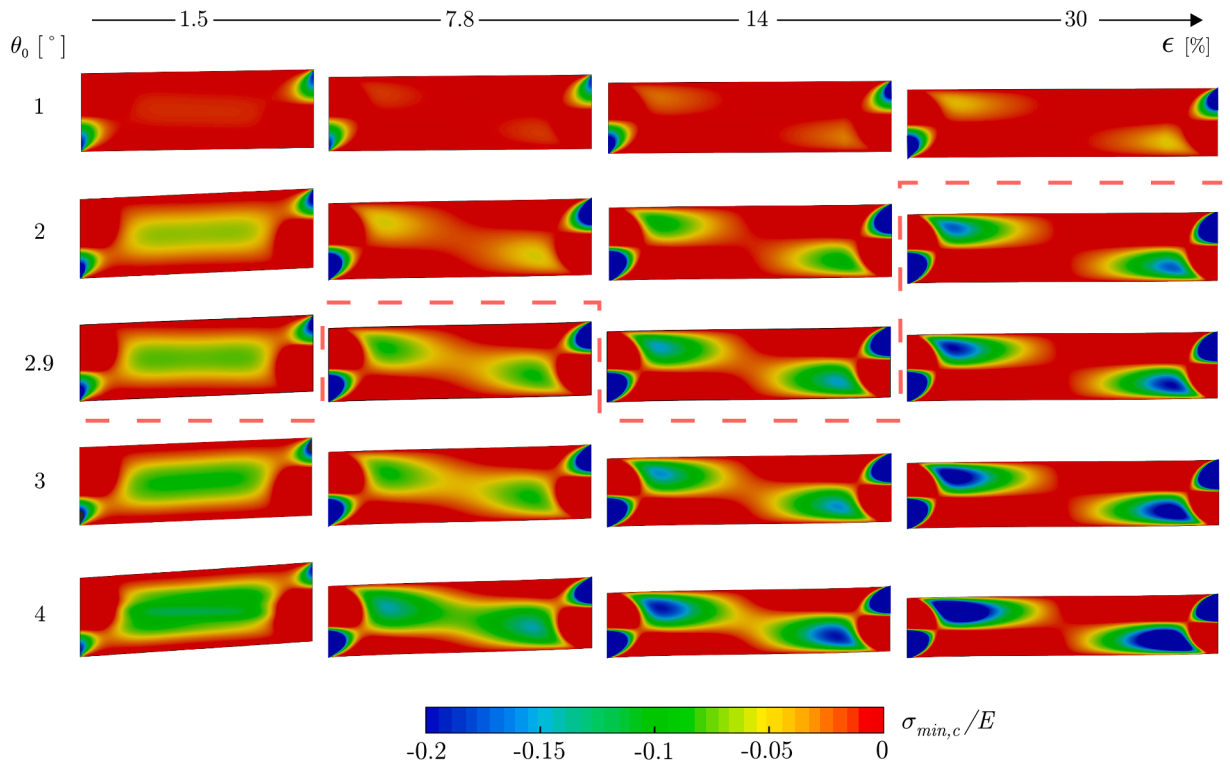

Fig. 8. Maps of the compressive (minimum negative) principal in-plane stress $\sigma_{min,c}$ (35) associated with the five compressible Neo-Hookean membranes displayed in Fig. 1, evaluated from FE simulations under planar configuration.

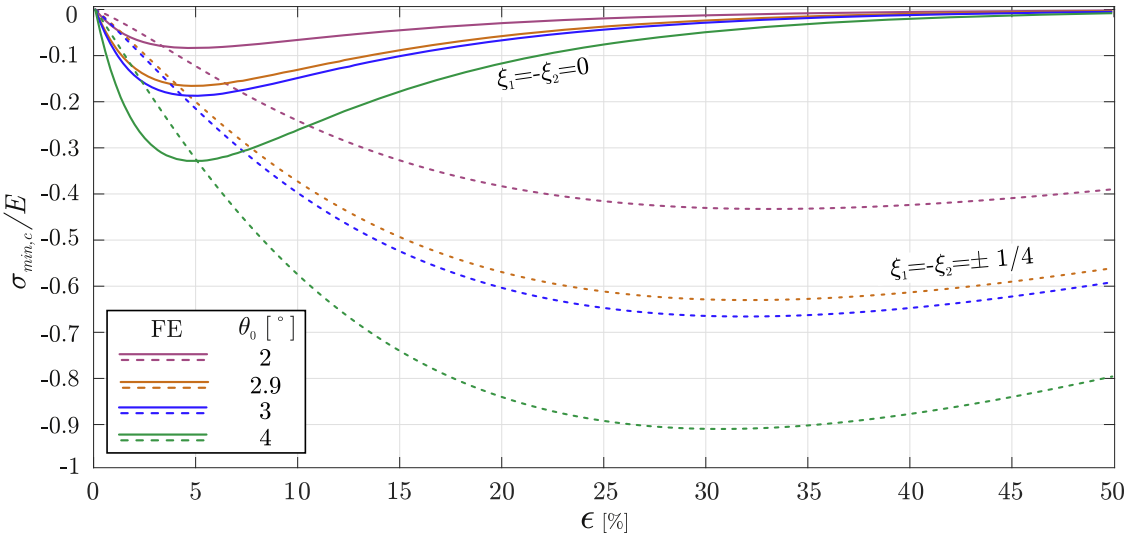

Fig. 9. Compressive (minimum negative) principal in-plane stress $\sigma_{min,c}$ at the center ($\xi_1 = \xi_2 = 0$) and at the quadrant centers ($\xi_1 = -\xi_2 = \pm 1/4$) evaluated from FE simulations (under planar configuration) as a function of the elongation strain ϵ for Neo-Hookean membranes of Fig. 8 at different initial inclination angle values $\theta_0 = \{2, 2.9, 3, 4\}°$.

range and the nonlinear response in ϵ, which is displayed only for large strain $\epsilon > 10\,\%$ at the quadrant centers ($\xi_1 = -\xi_2 = \pm 1/4$) but also for intermediate small deformations ($\epsilon > 3\,\%$) at the center ($\xi_1 = \xi_2 = 0$). The compressive stress exhibits a non-monotonic trend at both locations, although the reduction in its magnitude occurs at $\epsilon \approx 5\,\%$ for the center and at $\epsilon \approx 30\,\%$ for the quadrant centers. Moreover, while at small strains the compressive stress at the quadrant centers is around half of that at the center, at large strain the compressive stress becomes very small at the center and very large at the quadrant centers. The interplay of these nonlinear planar behaviours with the small bending stiffness of the membrane leads to the different scenarios for the wrinkling pattern evolution.

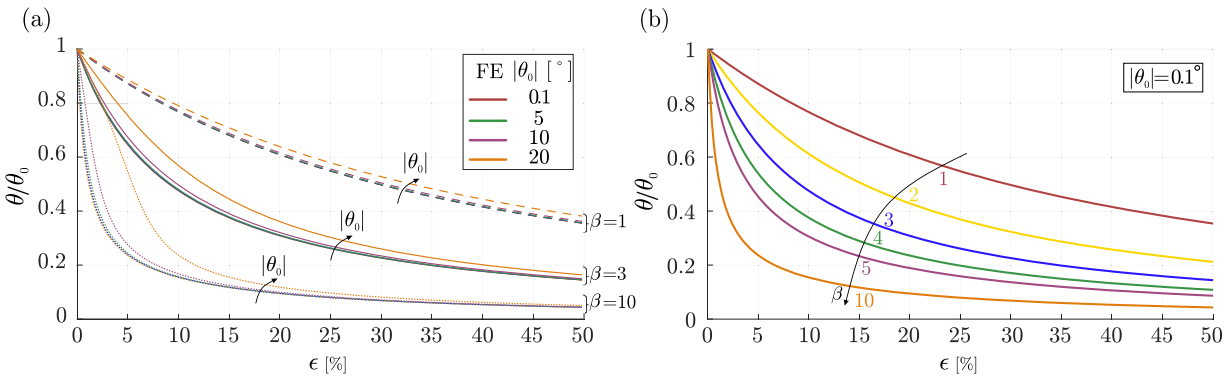

Fig. 10. Current inclination angle θ (37), normalized through division by its initial value θ_0, evaluated from FE simulations (under planar configuration) as a function of the elongation strain ϵ for (a) different moduli of the initial inclination angle $|\theta_0| = \{0.1, 1, 3, 5, 10, 20\}°$ and aspect ratios $\beta = \{1, 3, 10\}$ and for (b) initial inclination angle $|\theta_0| = 0.1°$ and different aspect ratios $\beta = \{1, 2, 3, 4, 5, 10\}$.

3.3.2. *Inclined edges realignment with x_1-axis during the stretching process*

During the elongation process, the parallelogram membrane modifies its shape towards a closer rectangular geometry, with its deformed free edges $\partial\mathbb{B}_{\mathbf{x}}^{[a]}$ and $\partial\mathbb{B}_{\mathbf{x}}^{[b]}$ reducing their inclination and becoming more aligned with the x_1-axis. To quantitatively assess this phenomenon, the current inclination angle θ is introduced as (Fig. 4)

$$\theta(\theta_0, \beta, \epsilon) = \arctan\left[\frac{1}{1+\epsilon}\left(\tan\theta_0 + \frac{u_2(\xi_1 = 1/2, \xi_2 = 0) - u_2(\xi_1 = -1/2, \xi_2 = 0)}{L}\right)\right] \in [0, \theta_0], \tag{37}$$

which measures the transition between the two limit cases, the undeformed parallelogram ($\theta = \theta_0$) and the limit rectangular shape ($\theta = 0$). The current inclination angle θ has been numerically evaluated from several simulations performed for six different moduli of the initial inclination angle $|\theta_0| = \{0.1, 1, 3, 5, 10, 20\}°$ and for three different aspect ratios $\beta = \{1, 3, 10\}$ and is reported in Fig. 10(a) with varying of the elongation strain ϵ. For completeness, the curves of the current inclination angle θ with varying the strain ϵ for $|\theta_0| = 0.1°$ and $\beta = \{1, 2, 3, 4, 5, 10\}$ are also reported in Fig. 10(b).

From Fig. 10(a), it can be concluded that, although the evolution law for the current inclination angle θ is highly nonlinear, the following linear expression holds for small initial inclination angles θ_0 (especially within the considered aspect ratio range $\beta \in [2, 5]$)

$$\lim_{\theta_0 \to 0} \theta(\theta_0, \beta, \epsilon) = \theta_0 R(\beta, \epsilon), \tag{38}$$

where $R(\beta, \epsilon) \in [0, 1]$ is a dimensionless function describing the reduction of the inclination angle magnitude due to both stretching and rigid-body motion. From Fig. 10(a), it is also noted that the function $R(\beta, \epsilon)$ is smooth and therefore can be expressed through a polynomial expression in ϵ truncated at the Mth power ($M \in \mathbb{N}$)

$$R(\beta, \epsilon) = 1 + \sum_{j=1}^{M} (-1)^j r_j(\beta)\, \epsilon^j. \tag{39}$$

From the theoretical point of view, the values for $r_j(\beta)$ can be obtained from the coefficients of the series expansion for $R(\beta, \epsilon)$ through its jth derivative as

$$r_j(\beta) = \frac{(-1)^j}{j!} \frac{\partial^j R(\beta, \epsilon)}{\partial \epsilon^j}, \qquad j \in \mathbb{N}. \tag{40}$$

Nevertheless, the $r_j(\beta)$ coefficients obtained through this approach exhibit diverging magnitudes, resulting in poor convergence even for small ranges of elongation strain ϵ. For this reason, alternatively, the coefficients $r_j(\beta)$ can be defined from curve fitting of the numerical results reported in Fig. 10 to maintain, although in an approximate way, a good representation still with small M values. As example, the coefficients $r_j(\beta)$ ($j = 1, 2, 3$) evaluated through curve fitting of the polynomial expression (39) for $R(\beta, \epsilon)$ limited to $M = 3$ with the numerical data within the elongation range $\epsilon \in [0, 10]\%$ are reported in Table 2 for different aspect ratio values $\beta = \{2, 3, 4, 5\}$.

It is finally highlighted that the magnitude of the current inclination angle θ strongly decreases even for limited small strain values, indeed for example at an elongation strain $\epsilon = 1\,\%$ (10 %) the current inclination angle θ differs from the initial value θ_0 by 5.3 % (38.4 %) when $\beta = 2$ and by 19.1 % (69 %) when $\beta = 5$.

3.4. *A fifth possible response: Edge wrinkling parallel to the x_2-axis displayed closely to the two acute-angled corners*

It is worth to mention that in addition to the four above-described behaviours ($\mathcal{O}$, $\mathcal{A}_1$, $\mathcal{B}_3$, $\mathcal{B}_1$), a fifth one exists. This additional response falls outside the $\beta - \theta_0$ domain reported in Fig. 7 and is associated to membrane geometries characterized by $\beta\theta_0 \gtrsim 1/3$. In this response the bifurcation from the flat state occurs through wrinkling parallel to the x_2-axis displayed closely to the two acute-angled corners. The response transition from region $\mathcal{B}_1$ to $\mathcal{C}$ is displayed in Fig. 11, where the maps of the out-of-plane displacement

Table 2
Values of the first three coefficients $r_j(\beta)$ $(j = 1, 2, 3)$ for different aspect ratio values $\beta = \{2, 3, 4, 5\}$ evaluated from cubic curve fitting of the numerical data in Fig. 10(b) within the elongation range $\epsilon \in [0, 10]\%$.

β	2	3	4	5
r_1	5.938	10.49	15.86	21.34
r_2	27.96	82.24	166.54	266.42
r_3	74.84	301.35	713.66	1245.4

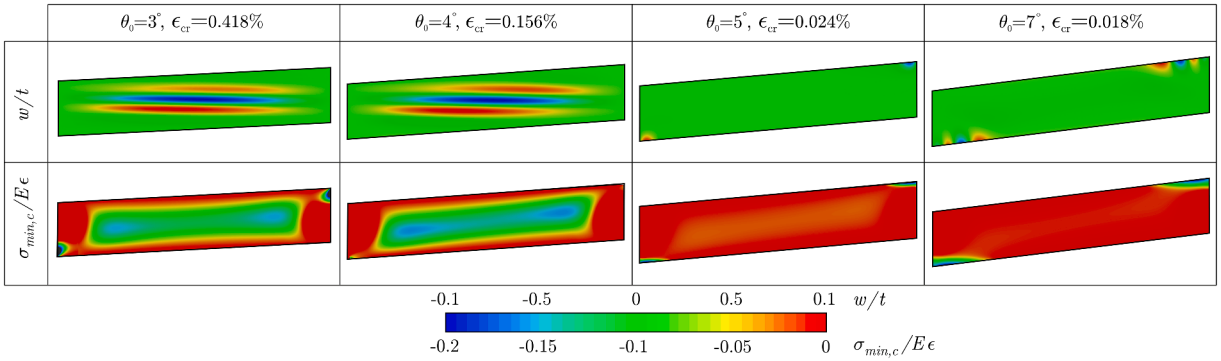

Fig. 11. Maps of the out-of-plane displacement $w(\mathbf{x})$ (first line) and of the compressive principal in-plane stress $\sigma_{min,c}(\mathbf{x})$ (second line) from FE simulations for a membrane with an aspect ratio $\beta = 5$ and increasing initial inclination angle $\theta_0 = \{3, 4, 5, 7\}°$ (from left to right) at the corresponding first critical elongation strain $\epsilon_{\rm cr}$. The first bifurcation occurs as central wrinkling parallel to the x_1-axis for $\theta_0 = 3°$ and 4°, and as edge wrinkling parallel to the x_2-axis close to the two acute-angled corners for $\theta_0 = 5°$ and 7°.

$w(\mathbf{x})$ and of the compressive principal in-plane stress $\sigma_{min,c}(\mathbf{x})$ are reported for a membrane with an aspect ratio $\beta = 5$ at increasing initial inclination angle $\theta_0 = \{3, 4, 5, 7\}°$ and corresponding first critical elongation strain ($\epsilon_{\rm cr} = \{0.418, 0.156, 0.0024, 0.018\}\%$). While the out-of-displacement maps show that the central wrinkling is no longer the first critical mode when $\theta_0 = 5°$ and 7°, the compressive principal stress maps highlight how the central region becomes relatively unloaded and how the state changes close to the two acute-angled corners with the increase of the inclination angle θ_0. An analytical explanation to this response is provided at the end of Section 4.1.

4. Analytical evaluation of the critical elongation strain for central wrinkling from perturbation approach and potential energy

With reference to a small parameter a (with $|a| \ll 1$), the total potential energy $\mathcal{V}$ associated with a small out-of-plane displacement $a\,\hat{w}(x_1, x_2)$ perturbing a flat ($w = 0$) equilibrated configuration described by the in-plane displacement $\widetilde{\boldsymbol{u}}(x_1, x_2)$ can be evaluated through the following second-order expansion in a

$$\mathcal{V}(\widetilde{\boldsymbol{u}}, a\hat{w}) \approx \mathcal{V}(\widetilde{\boldsymbol{u}}, 0) + a\,\mathcal{V}'(\widetilde{\boldsymbol{u}}, a\hat{w})\Big|_{a=0} + \frac{a^2}{2}\,\mathcal{V}''(\widetilde{\boldsymbol{u}}, a\hat{w})\Big|_{a=0}, \tag{41}$$

where the prime symbol ($'$) stands for derivative in a. Because of equilibrium, the first derivative vanishes, $\mathcal{V}'(\widetilde{\boldsymbol{u}}, a\hat{w})\Big|_{a=0} = 0$, while the second derivative $\mathcal{V}''(\widetilde{\boldsymbol{u}}, a\hat{w})\Big|_{a=0}$ follows from the generic expression of the total potential energy $\mathcal{V}$ (A.3) as (repeated indices imply summation)

$$\mathcal{V}''(\widetilde{\boldsymbol{u}}, a\hat{w})\Big|_{a=0} = \int_{\mathbb{B}_{\mathbf{x}}} \left(N_{\gamma\zeta}(\widetilde{\boldsymbol{u}})\,\frac{\partial\hat{w}}{\partial x_\gamma}\frac{\partial\hat{w}}{\partial x_\zeta} + \frac{\partial M_{\gamma\zeta}}{\partial\kappa_{\rho\sigma}}\bigg|_{\boldsymbol{\kappa}=\mathbf{0}} \frac{\partial^2\hat{w}}{\partial x_\gamma\partial x_\zeta}\frac{\partial^2\hat{w}}{\partial x_\rho\partial x_\sigma} \right) \mathrm{d}x_1\mathrm{d}x_2. \tag{42}$$

It follows that the stability of the flat configuration for the membrane is strictly connected to the sign of $\mathcal{V}''(\widetilde{\boldsymbol{u}}, a\hat{w})\Big|_{a=0}$, namely

$$\text{flat configuration } (w = 0) \text{ is } \begin{cases} \text{stable if } \mathcal{V}''(\widetilde{\boldsymbol{u}}, a\hat{w})\Big|_{a=0} > 0 \quad \forall\,\hat{w}, \\ \text{unstable otherwise,} \end{cases} \tag{43}$$

and therefore the critical elongation strain $\epsilon_{\rm cr}$ is associated with the annihilation condition for the second derivative,

$$\text{critical condition:} \qquad \mathcal{V}''(\widetilde{\boldsymbol{u}}, a\hat{w})\Big|_{a=0} = 0. \tag{44}$$

With reference to the linear response in bending, holding for the SVK $(19)_2$ and LE $(21)_2$ models, and reparameterizing the integral onto the unit square domain, the second derivative $\mathcal{V}''$ (42) can be rewritten as

$$\begin{aligned}\mathcal{V}''\left(\widetilde{\boldsymbol{u}}, a\widehat{w}\right)\Big|_{a=0} = \beta \int_{\mathbb{B}_\xi} \Bigg\{ & N_{11}\left(\widetilde{\boldsymbol{u}}\right)\left(\frac{1}{\beta}\frac{\partial \widehat{w}}{\partial \xi_1} - \tan\theta_0 \frac{\partial \widehat{w}}{\partial \xi_2}\right)^2 + N_{22}\left(\widetilde{\boldsymbol{u}}\right)\left(\frac{\partial \widehat{w}}{\partial \xi_2}\right)^2 + 2N_{12}\left(\widetilde{\boldsymbol{u}}\right)\frac{\partial \widehat{w}}{\partial \xi_2}\left[\frac{1}{\beta}\frac{\partial \widehat{w}}{\partial \xi_1} - \tan\theta_0 \frac{\partial \widehat{w}}{\partial \xi_2}\right] \\ & + \frac{D}{\beta^2 W^2}\Bigg[\left(\frac{1}{\beta}\frac{\partial^2 \widehat{w}}{\partial \xi_1^2} - 2\tan\theta_0 \frac{\partial^2 \widehat{w}}{\partial \xi_1 \partial \xi_2} + \beta\left(1+\tan^2\theta_0\right)\frac{\partial^2 \widehat{w}}{\partial \xi_2^2}\right)^2 \\ & -2(1-\nu)\left(\frac{\partial^2 \widehat{w}}{\partial \xi_1^2}\frac{\partial^2 \widehat{w}}{\partial \xi_2^2} - \left(\frac{\partial^2 \widehat{w}}{\partial \xi_1 \partial \xi_2}\right)^2\right)\Bigg]\Bigg\} \,\mathrm{d}\xi_1\,\mathrm{d}\xi_2.\end{aligned} \tag{45}$$

As the in-plane displacement $\widetilde{\mathbf{u}}$ and the membrane force $\mathbf{N}$ over the hyperelastic parallelogram and the out-of-plane displacement $\widehat{w}$ at wrinkling depend on the inclination angle θ_0, the following second-order expansions in θ_0 can be considered

$$\widetilde{\mathbf{u}}(\boldsymbol{\xi}) = \widetilde{\mathbf{u}}^{(0)}(\boldsymbol{\xi}) + \theta_0 \widetilde{\mathbf{u}}^{(1)}(\boldsymbol{\xi}) + \theta_0^2 \widetilde{\mathbf{u}}^{(2)}(\boldsymbol{\xi}), \qquad \mathbf{N}(\boldsymbol{\xi}) = \mathbf{N}^{(0)} + \theta_0 \mathbf{N}^{(1)}(\boldsymbol{\xi}) + \theta_0^2 \mathbf{N}^{(2)}(\boldsymbol{\xi}), \qquad \widehat{w}(\boldsymbol{\xi}) = \widehat{w}^{(0)}(\boldsymbol{\xi}) + \theta_0 \widehat{w}^{(1)}(\boldsymbol{\xi}) + \theta_0^2 \widehat{w}^{(2)}(\boldsymbol{\xi}), \tag{46}$$

from which the second-order expansion of the second derivative $\mathcal{V}''\left(\widetilde{\boldsymbol{u}}, a\widehat{w}\right)\Big|_{a=0}$ follows as

$$\mathcal{V}'' = \mathcal{V}''^{(0)} + \theta_0 \mathcal{V}''^{(1)} + \theta_0^2 \mathcal{V}''^{(2)}, \tag{47}$$

where the explicit expressions for $\mathcal{V}''^{(j)}$ $(j = 0, 1, 2)$ as functions of $\mathbf{N}^{(k)}(\boldsymbol{\xi})$ and $\widehat{w}^{(k)}(\boldsymbol{\xi})$ $(k = 0, 1, 2)$ are deferred to Appendix C. To further proceed with the identification of the critical elongation strain ϵ_{cr}, an approximation for $\mathbf{N}(\boldsymbol{\xi})$ has be disclosed and a class for $\widehat{w}(\boldsymbol{\xi})$ describing possible wrinkling patterns has to be introduced. As only the magnitude of the inclination angle θ_0, and not its sign, can affect the critical elongation strain ϵ_{cr} value, the first-order expansion of the second variation has to vanish

$$\mathcal{V}''^{(1)} = 0, \tag{48}$$

and the critical condition (44) reduces to

$$\mathcal{V}''^{(0)} + \theta_0^2 \mathcal{V}''^{(2)} = 0. \tag{49}$$

The evaluation of the membrane force $\mathbf{N}(\boldsymbol{\xi})$ and the critical condition for the potential energy second derivative $\mathcal{V}''$ are respectively addressed in the next two Subsections.

4.1. Approximate in-plane stress field for quasi-rectangular geometries through perturbation approach

Under the assumption of small-strain ($\mathbf{F} \approx \mathbf{I}$, $\det[\mathbf{F}] \approx 1$, $\mathbf{E}^{[m]} \approx \boldsymbol{\epsilon}^{[m]}$) and planar state ($w = 0$, $\mathbf{M} = \mathbf{0}$) the nonlinear relation (36) between membrane force $\mathbf{N}$ and the (planar) Cauchy stress $\boldsymbol{\sigma}$ reduces to $\boldsymbol{\sigma} = \mathbf{N}/t$ and therefore from the linearized constitutive response (21) the Cauchy stress $\boldsymbol{\sigma}$ is dependent on the membrane strain $\boldsymbol{\epsilon}^{[m]}$ by the linear elastic relation

$$\boldsymbol{\sigma} = \frac{E}{1-\nu^2}\left[\nu\,\mathrm{tr}\left(\boldsymbol{\epsilon}^{[m]}\right)\mathbf{I}_s + (1-\nu)\,\boldsymbol{\epsilon}^{[m]}\right]. \tag{50}$$

The Cauchy stress $\boldsymbol{\sigma}$ satisfies the linearized version of the equilibrium Eq. (11) and of the static boundary conditions (26) and (27)

$$\nabla_s \cdot \boldsymbol{\sigma} = \mathbf{0}, \qquad \text{for } x_1, x_2 \in \mathbb{B}_{\mathbf{x}}, \qquad \begin{cases} \boldsymbol{\sigma}\mathbf{n} = \mathbf{0}, & \text{for } x_1, x_2 \in \partial\mathbb{B}_{\mathbf{x}}^{[a]} \cup \mathbb{B}_{\mathbf{x}}^{[b]}, \\ \sigma_{12} = 0, & \text{for } x_1, x_2 \in \partial\mathbb{B}_{\mathbf{x}}^{[l]} \cup \mathbb{B}_{\mathbf{x}}^{[r]}, \end{cases} \tag{51}$$

while the in-plane displacement $\widetilde{\mathbf{u}}$ remains subject to the kinematic boundary conditions (28) and (29).

By assuming small values for θ_0, the Cauchy stress $\boldsymbol{\sigma}$ and the membrane strain $\boldsymbol{\epsilon}^{[m]}$ over the hyperelastic parallelogram, as well as the outward unit normals $\mathbf{n}$ (25), can be expanded at the second-order in the initial inclination angle θ_0 as

$$\boldsymbol{\sigma} = \boldsymbol{\sigma}^{(0)} + \theta_0 \boldsymbol{\sigma}^{(1)} + \theta_0^2 \boldsymbol{\sigma}^{(2)}, \qquad \boldsymbol{\epsilon}^{[m]} = \boldsymbol{\epsilon}^{[m](0)} + \theta_0 \boldsymbol{\epsilon}^{[m](1)} + \theta_0^2 \boldsymbol{\epsilon}^{[m](2)}, \qquad \mathbf{n} = \mathbf{n}^{(0)} + \theta_0 \mathbf{n}^{(1)} + \theta_0^2 \mathbf{n}^{(2)}, \tag{52}$$

where the strain-displacement (20), the stress-strain (50) and the stress-membrane force relations hold at the different orders. The described expansion considers the parallelogram domain $\mathbb{B}_{\mathbf{x}}$ as a perturbation of the corresponding rectangular domain by inclining its two sides parallel to the x_1 axis by the small (initial) inclination angle θ_0. Therefore, as the domain $\mathbb{B}_{\mathbf{x}}$ depends on θ_0, it is instrumental to perform the perturbation analysis by referring the mechanical fields to the unit square domain $\mathbb{B}_{\boldsymbol{\xi}}$, where the two domains are related through each other via the linear transformation (30), which can be approximated at the second order in θ_0 under the condition $\beta \ll 1/|\theta_0|$ as

$$\boldsymbol{\xi} = \frac{1}{W}\left(\begin{bmatrix} \frac{1}{\beta} & 0 \\ 0 & 1 \end{bmatrix} + \theta_0 \begin{bmatrix} 0 & 0 \\ -1 & 0 \end{bmatrix}\right)\mathbf{x}. \tag{53}$$

Performing the analysis by referring to the auxiliary (normalized) coordinate $\boldsymbol{\xi}$ does not only allow to define the differential problem on a non-varying domain with respect to the perturbation parameter θ_0, but also to have a simple boundary description (namely, each boundary portion is defined only one variable coordinate, while the other one is constant), in a similar vein of the recently introduced approach for treating tapered beams (Migliaccio and D'Annibale, 2025) and (Migliaccio and Ruta, 2020).

The indefinite equilibrium equations $(51)_1$ can be expressed at the different orders in θ_0 in the unit square domain $\mathbb{B}_\xi$ as

$$\sigma^{(0)}_{1j,1}+\beta\sigma^{(0)}_{2j,2}=0,\qquad \sigma^{(1)}_{1j,1}+\beta\sigma^{(1)}_{2j,2}=\beta\sigma^{(0)}_{1j,2}\ \text{(0)},\qquad \sigma^{(2)}_{1j,1}+\beta\sigma^{(2)}_{2j,2}=\beta\sigma^{(1)}_{1j,2},\qquad j=1,2, \tag{54}$$

and the (kinematic and static) boundary conditions (28) and $(51)_{2,3}$ as

$$\begin{cases}\sigma^{(0)}_{j2}\left(\xi_1,\xi_2=\pm\frac{1}{2}\right)=0,\\ \sigma^{(0)}_{12}\left(\xi_1=\pm\frac{1}{2},\xi_2\right)=0,\\ \widetilde{u}^{(0)}_1\left(\xi_1=-\frac{1}{2},\xi_2\right)=0,\\ \widetilde{u}^{(0)}_1\left(\xi_1=\frac{1}{2},\xi_2\right)=\epsilon L,\end{cases}\qquad \begin{cases}\sigma^{(1)}_{j2}\left(\xi_1,\xi_2=\pm\frac{1}{2}\right)=\sigma^{(0)}_{1j}\left(\xi_1,\xi_2=\pm\frac{1}{2}\right)\ \{E\epsilon,0\},\\ \sigma^{(2)}_{j2}\left(\xi_1,\xi_2=\pm\frac{1}{2}\right)=\sigma^{(1)}_{j1}\left(\xi_1,\xi_2=\pm\frac{1}{2}\right)+\frac{1}{2}\sigma^{(0)}_{j2}\left(\xi_1,\xi_2=\pm\frac{1}{2}\right)\ 0,\\ \sigma^{(k)}_{12}\left(\xi_1=\pm\frac{1}{2},\xi_2\right)=0,\\ \widetilde{u}^{(k)}_1\left(\xi_1=\pm\frac{1}{2},\xi_2\right)=0.\end{cases}\qquad j,k=1,2. \tag{55}$$

While solving the differential problem (54) complemented by the boundary conditions (55) is straightforward at the 0th order, as the solution is given by the uniform tension along ξ_1 (corresponding to a rectangular domain under uniform stretching with lateral contraction allowed), achieving the solution at the 1st and 2nd order becomes awkward. Indeed, the respective boundary conditions enforce a discontinuity of the tangential stress $\sigma^{(k)}_{12}$ $(k\geq 1)$ at each corner of the unit square $(\xi_1=\pm\xi_2=\pm 1/2)$, similarly to the Timoshenko paradox problem (Barber, 2002), and therefore an analytical solution could be only obtained through series expression. Nevertheless, an approximate evaluation of the higher-order solution can still be pursued by replacing the local annihilation of the tangential stress and of normal displacement, Eqs. $(55)_7$ and $(55)_8$, with corresponding global conditions along the interested edges

$$\int_{-1/2}^{1/2}\sigma^{(k)}_{12}(\xi_1=\pm 1/2,\xi_2)\mathrm{d}\xi_2=\int_{-1/2}^{1/2}\widetilde{u}^{(k)}_1(\xi_1=\pm 1/2,\xi_2)\mathrm{d}\xi_2=0,\qquad k=1,2, \tag{56}$$

providing a null value for either the resultant shear force and the average normal displacement on the two parallelogram edges parallel to $\mathbb{B}^{[l]}_\xi$ and $\mathbb{B}^{[r]}_\xi$. Under this assumption, the second-order expansion (with rotational symmetry of order 2) for the stress field is found to be provided by the following closed-form over the parallelogram domain $\mathbb{B}_\mathbf{x}$ through the expanded linear transformation (53), leading to (see Appendix D for details)

$$\begin{Bmatrix}\sigma_{11}(\mathbf{x})\\ \sigma_{12}(\mathbf{x})\\ \sigma_{22}(\mathbf{x})\end{Bmatrix}=E\,\epsilon\left(\begin{Bmatrix}1\\0\\0\end{Bmatrix}+\theta_0\begin{Bmatrix}-\frac{12x_1x_2}{W^2}\\ -\frac{1}{2}+\frac{6x_2^2}{W^2}\\ 0\end{Bmatrix}+\theta_0^2\begin{Bmatrix}1+\frac{\beta^2-3\nu}{2}+12\frac{x_1^2-2x_2^2}{W^2}-C\\ -\frac{24x_1x_2}{W^2}\\ -2+\frac{12x_2^2}{W^2}\end{Bmatrix}\right),\qquad \mathbf{x}\in\mathbb{B}_\mathbf{x}, \tag{57}$$

where C is a constant completing the description of the first-order in-plane displacement field $\widetilde{\mathbf{u}}^{(1)}$ and remains arbitrary in the present analysis as it is based on the integral boundary conditions (56).

The minimum principal stress component σ_{min} and its inclination ϕ with respect to the x_1-axis can be evaluated through expression (35) from the stress field $\boldsymbol{\sigma}(\mathbf{x})$ (57), which, as $\beta\ll 1/|\theta_0|$, result

$$\sigma_{min}=-\frac{9}{4}\left(1-\frac{4x_2^2}{W^2}\right)^2\theta_0^2E\epsilon<0\ \ (\text{if }\epsilon>0),\qquad \phi=\frac{\pi}{2}-\theta_0\left(\frac{1}{2}-\frac{6x_2^2}{W^2}\right)-\theta_0^2\left(5-\frac{12x_2^2}{W^2}\right)\frac{6x_1x_2}{W^2}. \tag{58}$$

Eq. (58) discloses a second-order compressive stress in the initial inclination angle θ_0 within a parallelogram under elongation $(\epsilon>0)$, with maximum magnitude for $x_2\approx 0$ and acting approximately parallel to the x_2-axis.

With regards to the C parameter, which would remain arbitrary from the present analytical method and defines only a second-order term in the stress component σ_{11}, a comparison of the numerical value of σ_{11} at $x_1=x_2=0$ from FE simulations with the corresponding value from the analytical expression $(57)_1$ for different $\beta\in[1,10]$ and $\theta_0\in\{0.2,10\}^\circ$ (and disregarding the possible effect of the Poisson's ratio ν) provides the following expression

$$C=-\frac{3}{4}\left(1-2\beta^2\right). \tag{59}$$

For this value of C, the displacement component u_2 that can be obtained from integration of the stress components (57) leads to the evaluation of the current inclination angle θ through expression (37) as

$$\theta\approx\theta_0\left[1-\epsilon\left(\frac{23}{12}+\beta^2\right)\right], \tag{60}$$

which is in excellent agreement with the linear trend of the numerical curves reported in Fig. 10 associated to small values of the elongation strain ϵ. It is also noted that the obtained analytical expression (60) for the current inclination angle θ implies the normalized derivative $1/\theta_0\left(\mathrm{d}\theta/\mathrm{d}\epsilon\right)\big|_{\epsilon=0}=-\left(23/12+\beta^2\right)$, confirming that the current inclination angle θ dramatically decrease for $\beta\gtrsim 2$.

As the closed-form expression (57) is obtained by disregarding the boundary layer effects associated with the edges $\partial\mathbb{B}^{[l]}_\mathbf{x}$ and $\partial\mathbb{B}^{[r]}_\mathbf{x}$, the corresponding prediction is expected to be mostly reliable far from such boundaries. As a comparison, the stresses σ_{11}, σ_{12}, σ_{22},

and σ_{min} (normalized through division by $E\epsilon$) are reported with varying $\xi_2 \in [-1/2, 1/2]$ for constant values of $\xi_1 = -\{3/8, 1/4, 1/8, 0\}$ as provided by Eqs. (57) and (58) and by the numerical simulations in Fig. 12. The results are shown for a parallelogram with aspect ratio $\beta = 3$ and an initial inclination angle $\theta_0 = 2.5°$ at two different elongation strains, $\epsilon = 1\,\%$ (left) and $5\,\%$ (right). The analytical representation of the stress components is fully confirmed by the FE results at $1\,\%$ except for σ_{22} and σ_{min} evaluated at $\xi_1 = -3/8$, as this is closest to the boundary $\partial\mathbb{B}_{\mathbf{x}}^{[j]}$ ($\xi_1 = -1/2$).

Differently, although still within the small strain regime, at $5\,\%$ the analytical predictions loses fidelity for σ_{12}, σ_{22}, and σ_{min} even for central coordinates ($\xi_1 = -1/4, -1/8$ and 0). This loss of reliability for the analytical solution is associated to the dramatic change in the current inclination angle θ (discussed in Section 3.3.2), which introduces strong nonlinearities in the mechanical response even under limited values of the elongation strain ϵ.

A further comment is also provided with reference to membranes with large aspect ratios β. Despite the obtained solution (57) is formally valid only for $\beta \ll 1/|\theta_0|$ as it is based on the transformation expansion (53), it is interesting to observe that the stress component σ_{11} truncated at the first-order in θ_0 evaluated at the two acute-angled corners is

$$\sigma_{11}(\xi_1 = \text{sign}[\theta_0]\xi_2 = \pm 1/2) = E\,\epsilon\big(1 - 3\beta|\theta_0|\big), \tag{61}$$

providing an hint about the possibility for a compressive stress parallel to the x_1 axis when $\beta > 1/(3|\theta_0|)$. In a rough sense, this is in agreement with the stress maps in Fig. 11 for the membrane with $\beta = 5$ and $\theta_0 = 5°$ and $7°$ (for which $\beta\theta_0 = 0.436$ and 0.611, respectively), associated with edge wrinkling parallel to the x_2-axis displayed closely to the two acute-angled corners (Section 3.4).

4.2. Analytical evaluation of the critical elongation strain ϵ_{cr}

As the in-plane membrane force has been determined in the previous Subsection, the critical condition (49) can be fully elucidated by selecting a specific out-of-plane displacement $\widehat{w}$. In general terms, the out-of-plane displacement $\widehat{w}$ can be introduced as the following linear superposition

$$\widehat{w}(\mathbf{x}) = \mathbf{H} \cdot \mathbf{h}(\mathbf{x}), \tag{62}$$

where $\mathbf{H}$ and $\mathbf{h}(\mathbf{x})$ are the vectors respectively collecting the amplitude H_j and the functions $h_j(\mathbf{x})$ ($j = 1, \ldots, N$, being N the number of functions considered as basis for $\widehat{w}$), the latter such that the kinematic boundary condition $(27)_2$ is satisfied and the first-order term $\mathcal{V}''^{(1)}$ of the potential energy vanishes, (48). Under representation (68), the second order expansion in θ_0 of the second derivative $\mathcal{V}''$, Eq. (47), is described by the following quadratic expression in $\mathbf{H}$

$$\mathcal{V}'' = \frac{E\,W}{\alpha^3\beta^3}\mathbf{H} \cdot \left\{\mathbf{K}_e^{(0)} + \alpha^2\beta^2\mathbf{K}_g^{(0)}\epsilon + \theta_0^2\left[\mathbf{K}_e^{(2)} + \alpha^2\beta^2\mathbf{K}_g^{(2)}\epsilon\right]\right\}\mathbf{H}, \tag{63}$$

where $\mathbf{K}_e^{(j)}$ and $\mathbf{K}_g^{(j)}$ are respectively the (normalized) elastic and geometric stiffness (symmetric $N \times N$) matrices at the jth order ($j = 0$ and 2). The critical condition (49) for the second derivative of the potential energy (63) defines a generalized eigenproblem where $\mathbf{H}$ is the eigenvector and the critical elongation strain ϵ_{cr} is the eigenvalue obtained by imposing the determinant annihilation

$$\det\left\{\mathbf{K}_e^{(0)} + \alpha^2\beta^2\mathbf{K}_g^{(0)}\epsilon_{\text{cr}} + \theta_0^2\left[\mathbf{K}_e^{(2)} + \alpha^2\beta^2\mathbf{K}_g^{(2)}\epsilon_{\text{cr}}\right]\right\} = 0. \tag{64}$$

Therefore, the critical condition (64) defines ϵ_{cr} as the root(s) of a polynomium of order N

$$\mathsf{c}_N\epsilon_{\text{cr}}^N + \mathsf{c}_{N-1}\epsilon_{\text{cr}}^{N-1} + \ldots + \mathsf{c}_2\epsilon_{\text{cr}}^2 + \mathsf{c}_1\epsilon_{\text{cr}} + \mathsf{c}_0 = 0, \tag{65}$$

with c_j ($j = 0, \ldots, N$) being coefficients depending on the elastic ($\mathbf{K}_e^{(0)}$ and $\mathbf{K}_e^{(2)}$) and geometric ($\mathbf{K}_g^{(0)}$ and $\mathbf{K}_g^{(2)}$) stiffness matrices.

In order to maintain simplicity in the treatment, the number N of functions $h_j(\mathbf{x})$ is considered as $N = 1$, in which case the matrices reduce to a single component, $\mathbf{K}_e^{(j)} = \mathsf{K}_e^{(j)}$ and $\mathbf{K}_g^{(j)} = \mathsf{K}_g^{(j)}$ ($j = 0, 2$), and the polynomial Eq. (65) reduces to a linear equation

$$\alpha^2\beta^2\left[\mathsf{K}_g^{(0)} + \theta_0^2\mathsf{K}_g^{(2)}\right]\epsilon_{\text{cr}} + \mathsf{K}_e^{(0)} + \theta_0^2\mathsf{K}_e^{(2)} = 0, \tag{66}$$

for which the critical elongation strain ϵ_{cr} follows as

$$\epsilon_{\text{cr}} = -\frac{\mathsf{K}_e^{(0)} + \theta_0^2\mathsf{K}_e^{(2)}}{\alpha^2\beta^2\left[\mathsf{K}_g^{(0)} + \theta_0^2\mathsf{K}_g^{(2)}\right]}. \tag{67}$$

Considering that the closed-form expression (57) for the in-plane stress state is accurate only in the central region and for small elongation strains ϵ (Fig. 12), the critical condition is therefore evaluated exclusively for the central wrinkling patterns numerically identified in Section 3.2. These appear as wrinkles oriented parallel to the x_1- axis in the undeformed configuration, with an amplitude that decays away from the origin ($x_1 = x_2 = 0$) along both the x_1 and x_2 axes. Therefore, the following expression for the function $h_1(\mathbf{x})$ is considered

$$h_1(\mathbf{x}) = \left[1 - \left(\frac{2x_1}{\beta W}\right)^2\right]^2 \cos^4\left(\frac{\pi x_2}{W}\right)\cos\left(n\pi\left(\frac{1}{2} + \frac{x_2}{W}\right)\right), \tag{68}$$

being n a positive number (not restricted to be natural) defining the wrinkling wavelength along x_2. Once the function h_1 is selected, the four elastic and geometric stiffness coefficients $\mathsf{K}_e^{(0)}(n)$, $\mathsf{K}_g^{(0)}(n)$, $\mathsf{K}_e^{(2)}(n)$, and $\mathsf{K}_g^{(2)}(n)$ can be evaluated as functions of n (in addition to

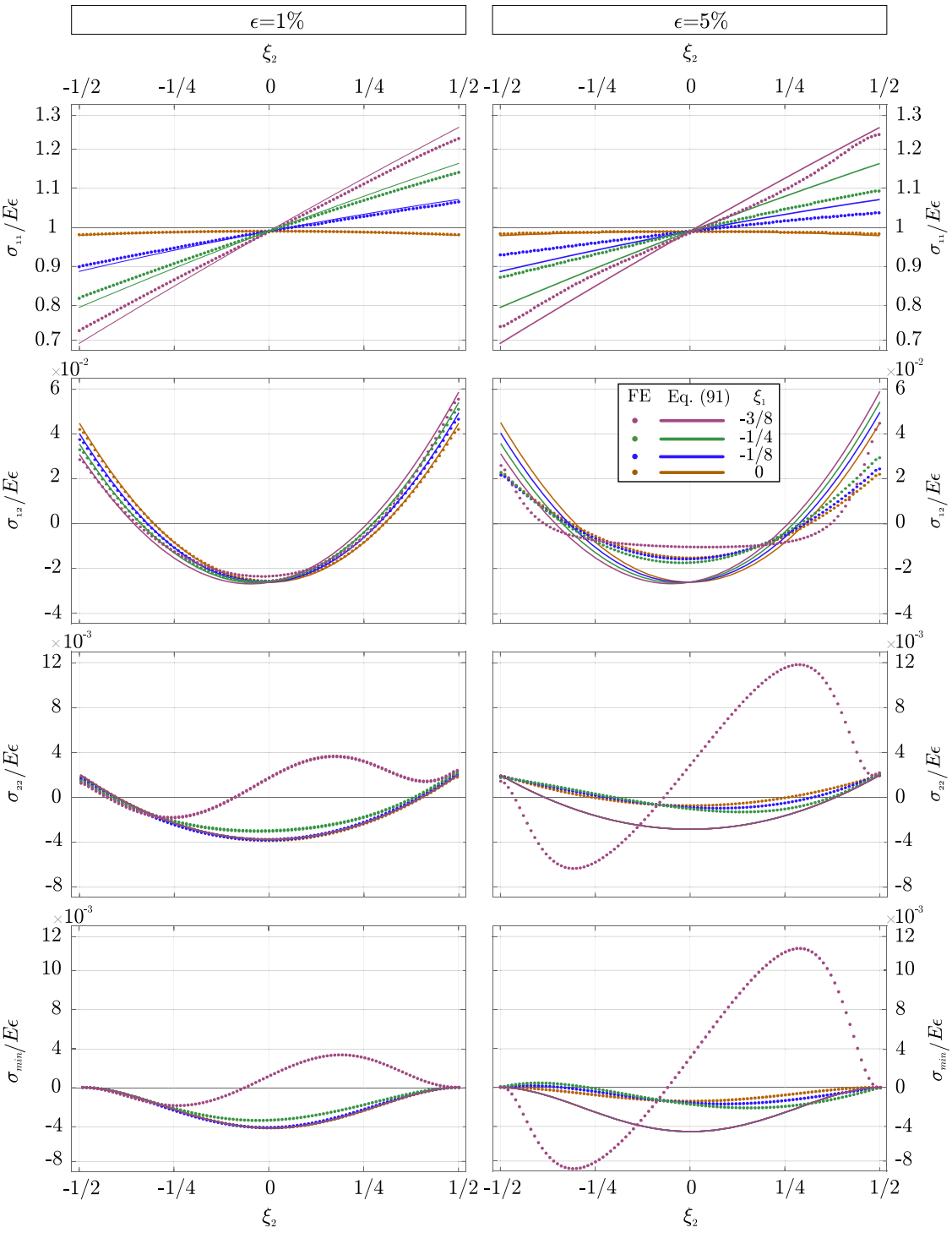

Fig. 12. Stress components σ_{11}, σ_{12}, σ_{22}, σ_{min} as functions of ξ_2, normalized through division by $E\epsilon$ and evaluated at $\xi_1 = -\{3/8, 1/4, 1/8, 0\}$. Continuous and dotted curves represent results respectively evaluated from the analytical expression (57) and the FE simulations for $\beta = 3$ and $\theta_0 = 2.5°$. Two elongation strains are considered, $\epsilon = 1\,\%$ (left columnn) and $5\,\%$ (right column).

the dimensionless membrane properties α, β, ν) and the critical elongation $\epsilon_{\mathrm{cr},n}(n)$ assessed from expression (67). While by definition $\mathsf{K}_e^{(0)}(n) > 0$, from the integration over the domain it is found that $\mathsf{K}_e^{(2)}(n) = 0\ \forall n$ and the expression (67) for the critical elongation strain ϵ_{cr} reduces to

$$\epsilon_{\mathrm{cr},n} = -\frac{\mathsf{K}_e^{(0)}(n)}{\alpha^2\beta^2\left[\mathsf{K}_g^{(0)}(n) + \theta_0^2\mathsf{K}_g^{(2)}(n)\right]}, \tag{69}$$

which, considering that from the domain integration it is found that $\mathsf{K}_g^{(0)}(n) > 0\ \forall n$, implies that the critical elongation strain is never positive for rectangular membranes, $\epsilon_{\mathrm{cr},n}(\theta_0 = 0) < 0\ \forall n$, and therefore confirming that no tension instability occurs for this limit geometry. However, the question remains if a non-vanishing inclination angle θ_0 may trigger or not the central wrinkling under elongation strain, $\epsilon_{\mathrm{cr}} > 0$. With this regard, it can be noted that whenever $\mathsf{K}_g^{(2)}(n) < 0$ then a corresponding critical elongation strain exists, $\epsilon_{\mathrm{cr},n} > 0$, for a sufficiently large inclination angle θ_0 (although within the small range). It follows that for a specific membrane material (ν) and geometry (α, β and θ_0), the critical elongation strain ϵ_{cr} can be evaluated through a minimization over the positive parameter n of the positive critical elongation strains $\epsilon_{\mathrm{cr},n} > 0$, namely

$$\epsilon_{\mathrm{cr}}(\theta_0,\alpha,\beta,\nu) = \min_{n\in\mathbb{R}^+}\left[\epsilon_{\mathrm{cr},n}(\theta_0,\alpha,\beta,\nu,n)\right], \qquad \text{restricted to } \epsilon_{\mathrm{cr},n}(\theta_0,\beta,\alpha,\nu,n) > 0. \tag{70}$$

Leaving the minimization over the whole set of positive values for n to specific membrane geometry and material, in the case of natural values of n the following closed-form expressions for the critical elongation strain $\epsilon_{\mathrm{cr},n}$ can be obtained as

$$\begin{aligned}
\epsilon_{\mathrm{cr},n=1} &= -\frac{50\pi^2}{(1-\nu^2)\alpha^2\beta^2}\,\frac{679\pi^4\beta^4 + 1320\pi^2\beta^2 + 3528}{50400\pi^2 - \theta_0^2\left(175\pi^2\left(1549\beta^2 + 432\nu + 72\right) + 33000\pi^4\beta^2 - 643272\right)},\\
\epsilon_{\mathrm{cr},n=2} &= -\frac{100\pi^2}{(1-\nu^2)\alpha^2\beta^2}\,\frac{386\pi^4\beta^4 + 732\pi^2\beta^2 + 3087}{88200\pi^2 - \theta_0^2\left(7\pi^2\left(52267\beta^2 + 3150(6\nu+1)\right) + 36600\pi^4\beta^2 - 1627206\right)},\\
\epsilon_{\mathrm{cr},n=3} &= -\frac{2450\pi^2}{(1-\nu^2)\alpha^2\beta^2}\,\frac{7663\pi^4\beta^4 + 9384\pi^2\beta^2 + 15624}{10936800\pi^2 - \theta_0^2\left(49\pi^2\left(2064019\beta^2 + 55800(6\nu+1)\right) + 11495400\pi^4\beta^2 - 168194184\right)},\\
\epsilon_{\mathrm{cr},n=4} &= -\frac{9800\pi^2}{(1-\nu^2)\alpha^2\beta^2}\,\frac{4288\pi^4\beta^4 + 3840\pi^2\beta^2 + 4473}{12524400\pi^2 - \theta_0^2\left(20\pi^2\left(8318078\beta^2 + 156555(6\nu+1)\right) + 18816000\pi^4\beta^2 - 220379757\right)},\\
\epsilon_{\mathrm{cr},n\geq 5} &= -\frac{2\pi^2n^2}{5(1-\nu^2)\alpha^2\beta^2}\,\frac{17640 + 120\pi^2\beta^2\left(7n^2+16\right) + \pi^4\beta^4\left(35n^4 + 480n^2 + 512\right)}{2016\pi^2n^2 - \theta_0^2 G_n(\beta,\nu)},
\end{aligned} \tag{71}$$

where $G_n(\beta,\nu)$ is defined for $n \in \mathbb{N}^+$ and with $n \geq 5$ by

$$\begin{aligned}
G_n(\beta,\nu) = \quad & \left[-382205952\left(2\pi^2\beta^2 - 21\right) + 7\pi^2\left(205 + 24\pi^2\right)\beta^2n^{20} - 4n^{18}\left(\pi^2\left(\left(20489 + 2424\pi^2\right)\beta^2\right.\right.\right.\\
& \left.\left.\left. -126(6\nu+1)\right) + 8610\right) + 18n^{16}\left(35\pi^2\left(2899\beta^2 - 288\nu - 48\right) + 12216\pi^4\beta^2 + 114800\right)\right.\\
& -4n^{14}\left(\pi^2\left(\left(4966619 + 618024\pi^2\right)\beta^2 - 182196(6\nu+1)\right) + 12450060\right)\\
& +n^{12}\left(\pi^2\left(\left(104529355 + 14060328\pi^2\right)\beta^2 - 9082080(6\nu+1)\right) + 620608800\right)\\
& -72n^{10}\left(3\pi^2\left(\left(805483 + 153096\pi^2\right)\beta^2 - 291389(6\nu+1)\right) + 59734745\right)\\
& -16n^8\left(\pi^2\left(\left(37922381 + 1212312\pi^2\right)\beta^2 + 15191820(6\nu+1)\right) - 1045945908\right)\\
& +128n^6\left(\pi^2\left(2\left(12034225 + 860424\pi^2\right)\beta^2 + 3885903(6\nu+1)\right) - 288398145\right)\\
& -36864n^4\left(\pi^2\left(4\left(36065 + 2082\pi^2\right)\beta^2 + 12915(6\nu+1)\right) - 1398495\right)\\
& \left.+2654208n^2\left(\pi^2\left(2\left(865 + 24\pi^2\right)\beta^2 + 63(6\nu+1)\right) - 17220\right)\right] \Big/ \left[\left(n^2-1\right)\left(n^2-4\right)\left(n^2-9\right)\left(n^2-16\right)\right]^2.
\end{aligned} \tag{72}$$

The critical elongation strain $\epsilon_{\mathrm{cr},n}$ obtained from the closed-form expressions (71) is reported at varying natural values of n as a function of the absolute value of the inclination angle $|\theta_0|$ for $\alpha = 1500$ and $\nu = 0.33$ in Fig. 13 for different $\beta = \{2,3,4,5\}$.

Each curve associated to a different n is reported as dashed except for the continuous portion representative of the minimum within the set of considered n. The natural value n providing the minimization is highlighted below the horizontal axis label for the corresponding ranges of θ_0. This information shows how the wrinkling wavelength (which is inversely proportional to n) decreases with the decrease of the aspect ratio β and of the initial inclination angle $|\theta_0|$.

The union of the minimum curve portions associated with natural values of n approximately represents the envelope ϵ_{cr} that would be obtained by performing the minimization over the positive set values for n as described by Eq. (70). The critical conditions numerically evaluated from the FE model are also included as circles in this Figure. Two types of circles are reported: blue circles, associated to wrinkling parallel to the x_1-axis in the membrane center (as observed for $\mathcal{B}_1$ and $\mathcal{B}_3$), and red circles, associated to wrinkling parallel to the x_2-axis at the two acute-angled corners (as observed for C). The comparison confirms the high reliability of the present analytical method in predicting the critical elongation strain for central wrinkling. Despite its simplicity, the analytical estimation of ϵ_{cr} closely matches the numerical evaluation (represented by blue circles), with a very limited relative error that increases as the critical elongation strain ϵ_{cr} grows. This is consistent with the observation that due to nonlinearities the analytical description of the planar stress loses fidelity, especially when the membrane geometry is close the transition between $\mathcal{A}_3$ and $\mathcal{B}_3$. Indeed, with reference to the comparison reported in Fig. 13, a maximum relative error of $\approx 15\,\%$ is attained for the case $\beta = 2$, $\theta_0 = 2.8°$ (which is close the transition between $\mathcal{A}_3$ and $\mathcal{B}_3$) and providing $\epsilon_{\mathrm{cr}} \approx 2.3\,\%$.

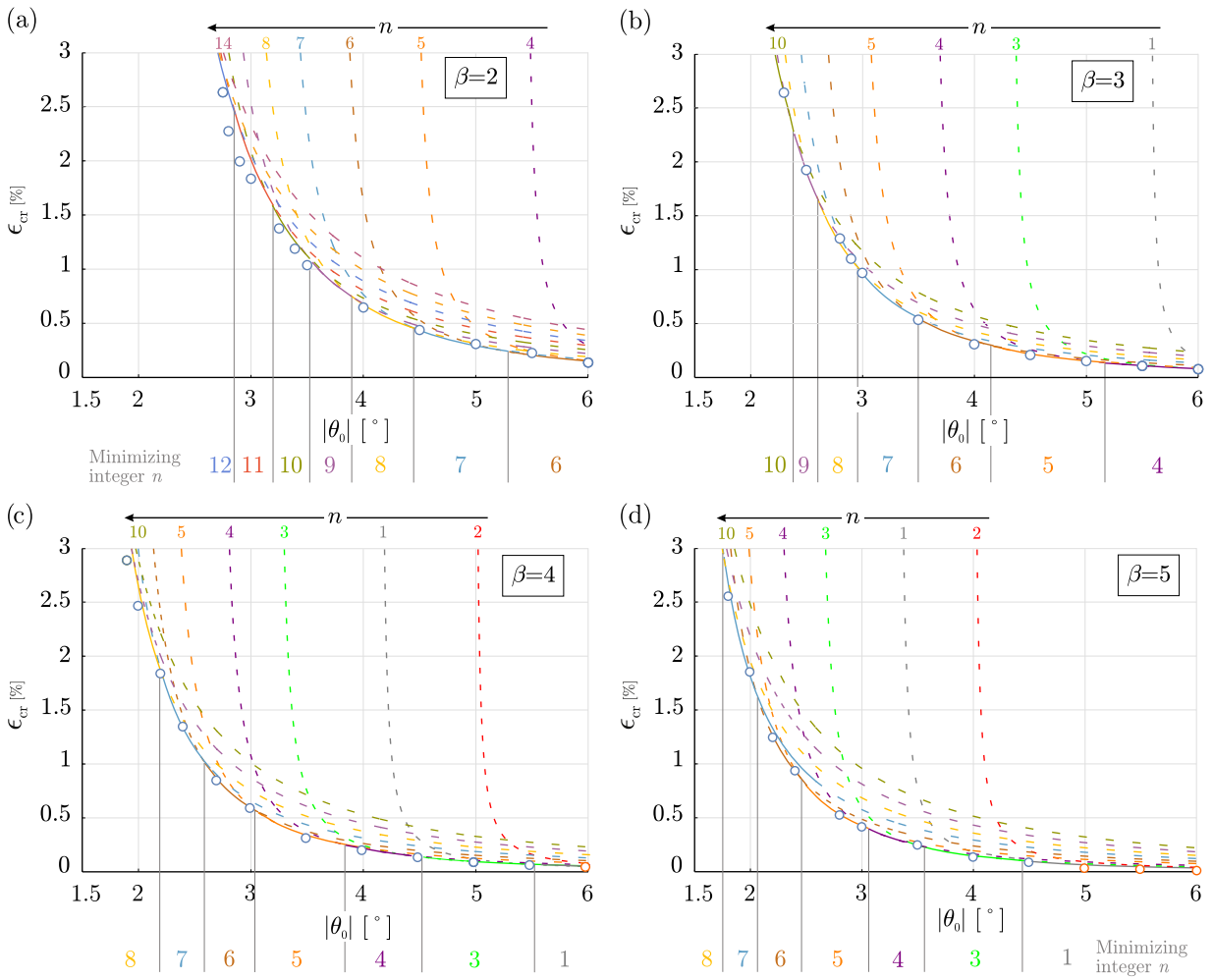

Fig. 13. Critical elongation strain ϵ_{cr} from Eq. (69) as a function of the initial inclination angle θ_0 for β =2(a), 3(b), 4(c) and 5(d). Different curves $\epsilon_{cr,n}$ (71) are reported as evaluated for different natural values of n. The portion of the curve associated with the minimizing natural n is reported as continuous, while the remaining non-minimizing part is dashed. The minimizing natural n is highlighted below the horizontal axis label. As a comparison with the analytical curves, the values of the critical elongation strain ϵ_{cr} obtained from FE solver at first bifurcation are also reported as circles, confirming the high reliability of the present analytical approach. Blue circles identify central wrinkling pattern, while red circles identify edge wrinkling pattern described in Section 3.4.

Furthermore, in addition to the validation of the critical value ϵ_{cr}, the comparison between the FE simulation and the analytical approach is also performed in terms of the wrinkling patterns in Fig. 2. Keeping the same parameters of Fig. 13 ($\alpha = 1500$, $\nu = 0.33$), four different geometries are analyzed: $\beta = 2$ with $\theta_0 = 3°$ and $5°$, $\beta = 3$ with $\theta_0 = 5°$, and $\beta = 5$ with $\theta_0 = 3°$. Also with regard to the wrinkling pattern, the comparison shows an excellent agreement between the analytical method and the FE numerical results.

A final comment is warranted for the geometries where the minimizing natural value of n is less than 4. In these cases, although the analytically predicted value of the critical elongation ϵ_{cr} agrees well with the corresponding numerical results, the wrinkling pattern predicted by the present analytical method does not fully match the numerical observations. This discrepancy can be attributed to a loss of reliability in the stress fields given by (57), since these geometries violate the underlying assumption $\beta|\theta_0| \ll 1$, and are thus close to – or even exactly – those that lead to edge wrinkling parallel to the x_2-axis at the two acute-angled corners, as discussed in Section 3.4.

5. Conclusions

The nonlinear mechanics and the wrinkling instability of initially flat, parallelogram-shaped hyperelastic membranes has been thoroughly analyzed. More specifically, with reference to a stretching boundary-value problem, usually not considered in membrane wrinkling as the lateral contraction is allowed, the role of geometry has been mainly investigated in terms of the (in-plane) aspect ratio β and of the initial inclination angle θ_0, the latter defining the deviation from the rectangular geometry. Unlike the more symmetric

setups commonly examined, the considered problem exhibits only second-order rotational symmetry, leading to a richer and more intricate mechanical response.

From nonlinear FE simulations recalling the geometrically extended version of the Föppl–von Kármán model, it has been found that:

- despite the apparent simplicity of the considered boundary-value problem, the elastic response is strongly affected by nonlinearities even at limited elongation strain levels ($2\,\% \lesssim \epsilon \lesssim 5\,\%$), as large variations in the current inclination angle θ take place (Fig. 10);
- while no instability under elongation is displayed in the limit case of rectangular geometry ($\theta_0 = 0$), wrinkling instability occurs for parallelogram geometries even at small initial inclination angle ($2^\circ \lesssim |\theta_0| \lesssim 3^\circ$), depending on the aspect ratio β;
- disregarding geometries ($\beta|\theta_0| \gtrsim 1/3$) for which edge wrinkling parallel to the x_2-axis may be experienced at the two acute-angled corners (Fig. 11), three main types of evolution involving wrinkling parallel to the x_1-axis are possible under a monotonic elongation process. By increasing the magnitude of the initial inclination angle $|\theta_0|$, these are correspondingly provided by (Fig. 1)

$\mathcal{A}_1$) wrinkling appearance only at large strains ($\epsilon \geq 10\,\%$), with the wrinkles displayed near the two obtuse-angled corners;

$\mathcal{B}_3$) wrinkling appearance at small strains ($\epsilon \in [1, 3]\%$), with wrinkle displayed in the central region. After an initial increase, with further elongation the wrinkle amplitude decreases until vanishing, indicating the restabilization of the flat configuration. After this circumstance, a second emergence of wrinkling eventually occurs for an additional increase in elongation. This second wrinkle is displayed near the two obtuse-angled corners;

$\mathcal{B}_1$) wrinkling appearance at very small strains ($\epsilon \lesssim 1\,\%$) displayed in the central region that never completely disappears but instead separates and migrates towards the two obtuse-angled corners through shape-morphing with the stretching increase.

Focusing on a linear elastic response, the investigation is also complemented by the following analytical results, which are relevant for limited small strains ($\epsilon \lesssim 3\,\%$):

- the stress fields have been evaluated as second-order expansion in the initial inclination angle θ_0 through application of the perturbation approach, Eq. (57). The approach has been applied with reference to a unit square domain where the parallelogram membrane is projected. As the boundary conditions on the edges parallel to the x_2-axis are implemented in integral sense, the achieved stress fields are approximate. A compressive stress emerges as a second-order effect in the initial inclination angle θ_0, oriented nearly parallel to the x_1-axis and attaining its maximum value at $x_2 = 0$, Eq. (58);
- the wrinkling condition has been effectively characterized in terms of both critical elongation strain and the corresponding wrinkling pattern (Figs. 2 and 13). The analytical prediction has been obtained through the application of the energy method, utilizing a single function for the out-of-plane displacement, which depends on the positive parameter n that defines the wrinkling wavelength along the x_2-axis. The wrinkling pattern at the bifurcation has been determined by minimizing the critical deformation value with respect to n. This approach yields a relatively simple closed-form expression (71).

In conclusion, beside introducing a new family of stretching boundary-value problems with allowed lateral contraction and a methodology for their resolution, the present investigation revealed the broad wrinkling landscape displayed by membranes slightly perturbed from the rectangular geometry. The possibility of wrinkling migration from one region to another within the membrane surface has been shown with increasing elongation strain. The analysis has been complemented by a closed-form expression predicting the critical elongation strain for which wrinkling in the central region occurs.

As practical outcome of the present investigation, a new design tool is provided for avoiding or tuning wrinkling instabilities in various technological fields, spanning from lightweight structures to flexible electronics and biomedical devices.

CRediT authorship contribution statement

Mohammad Hosein Nejabatmeimandi: Writing – review & editing, Writing – original draft, Visualization, Validation, Software, Methodology, Investigation, Formal analysis, Data curation; **Francesco Dal Corso:** Writing – review & editing, Writing – original draft, Visualization, Validation, Supervision, Software, Resources, Project administration, Methodology, Investigation, Funding acquisition, Formal analysis, Conceptualization.

Data availability

Data will be made available on request.

Declaration of competing interest

The authors declare that they have no known competing financial interests or personal relationships that could have appeared to influence the work reported in this paper.

Acknowledgment

MHN gratefully acknowledges financial support from the European Union's Horizon 2020 research and innovation programme under the Marie Skłodowska-Curie grant agreement No 956547. FDC gratefully acknowledges financial support from the European

Union, ERC grant HE GA 101,086,644 S-FOAM. Views and opinions expressed are however those of the authors only and do not necessarily reflect those of the European Union or the European Research Council Executive Agency. Neither the European Union nor the granting authority can be held responsible for them. The methodologies developed in the present work fall within the aims of the GNFM (Gruppo Nazionale per la Fisica Matematica) of the INDAM (Istituto Nazionale di Alta Matematica).

Appendix A. Details of the mechanical model

A.1. Green-Lagrange strain decomposition

The (symmetric) tensors $\mathbf{E}^{[\chi]}$ and $\mathbf{E}^{[q]}$ appearing in the decomposition (3) of the Green-Lagrange strain tensor $\mathbf{E}$ have components given by

$$\mathbf{E}^{[\chi]} = \begin{bmatrix} \kappa_{11} & \kappa_{12} & -\dfrac{w_{,1}\kappa_{11} + w_{,2}\kappa_{12}}{2} \\ \kappa_{12} & \kappa_{22} & -\dfrac{w_{,1}\kappa_{12} + w_{,2}\kappa_{22}}{2} \\ -\dfrac{w_{,1}\kappa_{11} + w_{,2}\kappa_{12}}{2} & -\dfrac{w_{,1}\kappa_{12} + w_{,2}\kappa_{22}}{2} & 0 \end{bmatrix}, \qquad \mathbf{E}^{[q]} = \begin{bmatrix} \kappa_{11}^2 + \kappa_{12}^2 & \kappa_{12}\left(\kappa_{11} + \kappa_{22}\right) & 0 \\ \kappa_{12}\left(\kappa_{11} + \kappa_{22}\right) & \kappa_{12}^2 + \kappa_{22}^2 & 0 \\ 0 & 0 & 0 \end{bmatrix}, \tag{A.1}$$

while the components of $\mathbf{E}^{[p]}$ are given in (6) and by

$$E_{13}^{[p]} = \frac{\widetilde{u}_{1,1}w_{,1} + \widetilde{u}_{1,2}w_{,2}}{2}, \qquad E_{23}^{[p]} = \frac{\widetilde{u}_{2,1}w_{,1} + \widetilde{u}_{2,2}w_{,2}}{2}, \qquad E_{33}^{[p]} = \frac{\left(w_{,1}\right)^2 + \left(w_{,2}\right)^2}{2}. \tag{A.2}$$

A.2. Membrane equilibrium equations from variational approach

Under kinematic and stress-free boundary conditions, the total potential energy $\mathcal{V}$ for the membrane is coincident with the stored elastic energy and therefore, due to the extended Föppl-von Kármán approximation (5), is given by

$$\mathcal{V} = \int_{\mathbb{B}_\mathbf{x}} \left[\Psi^{[m]}\left(\mathbf{E}^{[m]}\right) + \Psi^{[b]}\left(\mathbf{E}^{[m]}, \boldsymbol{\kappa}\right)\right] \mathrm{d}A. \tag{A.3}$$

The governing equations for the membrane can be obtained through the annihilation of the first variation $\delta\mathcal{V}$ of the total potential energy $\mathcal{V}$ (A.3) that, by considering the constitutive hyperelastic response (9), follows as

$$\delta\mathcal{V} = \int_{\mathbb{B}_\mathbf{x}} \left(\mathbf{N} \cdot \delta\mathbf{E}^{[m]} + \mathbf{M} \cdot \delta\boldsymbol{\kappa}\right) \mathrm{d}A, \tag{A.4}$$

where $\delta\mathbf{E}^{[m]}$ and $\delta\boldsymbol{\kappa}$ are compatible variations of the corresponding membrane Green-Lagrange strain $\mathbf{E}^{[m]}$ and curvature $\boldsymbol{\kappa}$ tensors. The first variation $\delta\mathcal{V}$ (A.4) can be rewritten as

$$\delta\mathcal{V} = \int_{\mathbb{B}_\mathbf{x}} \left\{-\mathbf{M} \cdot \nabla_s^2 \delta w + \frac{\mathbf{N}}{2} \cdot \left[\nabla_s \delta\widetilde{\mathbf{u}} + \left(\nabla_s \delta\widetilde{\mathbf{u}}\right)^T + \left(\nabla_s \delta\widetilde{\mathbf{u}}\right)^T \nabla_s \widetilde{\mathbf{u}} + \left(\nabla_s \widetilde{\mathbf{u}}\right)^T \nabla_s \delta\widetilde{\mathbf{u}} + \nabla_s \delta w \otimes \nabla_s w + \nabla_s w \otimes \nabla_s \delta w\right]\right\} \mathrm{d}A \tag{A.5}$$

which, after integration by parts, becomes

$$\begin{aligned} \delta\mathcal{V} = & \int_{\mathbb{B}_\mathbf{x}} \left\{-\nabla_s \cdot \left(\nabla_s \cdot \mathbf{M} + \mathbf{N}\nabla_s w\right)\delta w + \left[\nabla_s \cdot \left(\left(\mathbf{I}_s + \nabla_s \widetilde{\mathbf{u}}\right)\mathbf{N}\right)\right] \cdot \delta\widetilde{\mathbf{u}}\right\} \mathrm{d}A + \sum_{j=1}^{M} \left[\!\left[\mathbf{n} \cdot \mathbf{M}\mathbf{t}\right]\!\right] \delta w\big|_{\Gamma_j} \\ & + \int_{\partial\mathbb{B}_\mathbf{x}} \left\{-\left(\mathbf{n} \cdot \mathbf{M}\mathbf{n}\right)\left(\nabla_s \delta w\right) \cdot \mathbf{n} + \left[\mathbf{N}\nabla_s w + \nabla_s \cdot \mathbf{M} + \mathbf{t} \cdot \left(\nabla_s(\mathbf{M}\mathbf{t})\right)\right] \cdot \mathbf{n}\delta w + \left[\left(\mathbf{I}_s + \nabla_s \widetilde{\mathbf{u}}\right)\mathbf{N}\mathbf{n}\right] \cdot \delta\widetilde{\mathbf{u}}\right\} \mathrm{d}a. \end{aligned} \tag{A.6}$$

The annihilation of the first variation $\delta\mathcal{V}$ (A.4) for every compatible displacement variations $\delta\widetilde{\mathbf{u}}$ and δw implies the set of indefinite equilibrium Eq. (11) complemented by the boundary (12) and corner (13) conditions.

Appendix B. Comparison of critical and post-critical responses for NH and SVK models

A comparison of membranes modeled with Neo-Hookean (NH) and Saint-Venant–Kirchhoff (SVK) hyperelasticity is reported in Fig. B.1. The maximum absolute value of the out-of-plane displacement over the membrane domain w_{max} with increasing elongation strain ϵ is reported on the left for $\alpha = 2000$, $\beta = 3$, $E = 200$ MPa and $\nu = 0.4$ and two different inclination angles $\theta_0 = 2°$ and $3°$. The critical elongation strain values ϵ_{cr} as function of the initial inclination angle θ_0 are reported on the right for $\alpha = 1500$, $\beta = 3$, $E = 200$ MPa and $\nu = 0.4$. Both comparisons confirm that the two hyperelastic models display the same qualitative response.

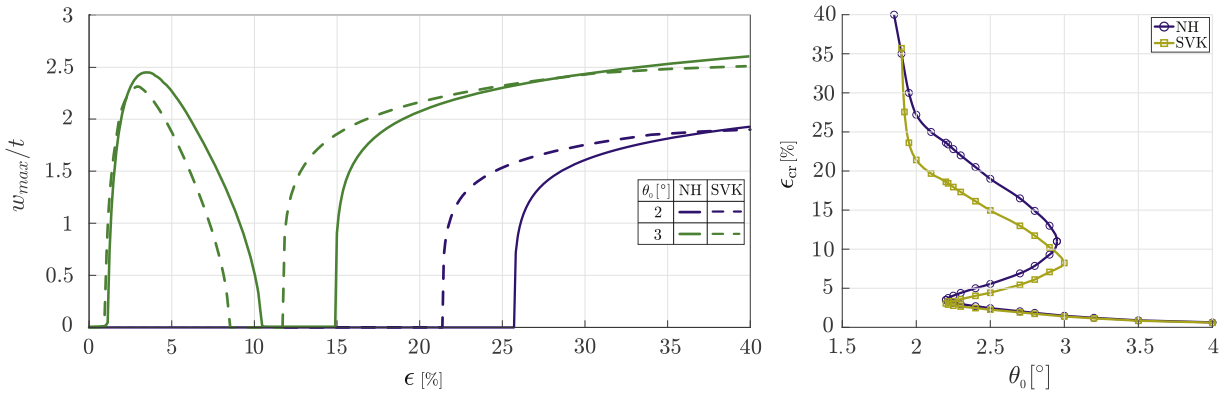

Fig. B.1. Qualitatively coincident response of membranes modeled as Neo-Hookean (NH) and Saint Venant–Kirchhoff (SVK). (Left) Maximum absolute value of the out-of-plane displacement over the membrane domain w_{max} with increasing elongation strain ϵ for $\alpha = 2000$, $\beta = 3$, $E = 200$ MPa and $\nu = 0.4$ and two different inclination angles $\theta_0 = 2°$ and $3°$. (Right) The critical elongation strain values ϵ_{cr} with varying the initial inclination angle θ_0 for $\alpha = 1500$, $\beta = 3$, $E = 200$ MPa and $\nu = 0.4$.

Appendix C. Expansion terms $\mathcal{V}''^{(0)}$, $\mathcal{V}''^{(1)}$, and $\mathcal{V}''^{(2)}$ of the second derivative $\mathcal{V}''$

The terms $\mathcal{V}''^{(0)}$, $\mathcal{V}''^{(1)}$, and $\mathcal{V}''^{(2)}$ defining the expansion (47) for the second derivative $\mathcal{V}''(\tilde{\boldsymbol{u}}, a\hat{w})\big|_{a=0}$ are given by

$$\mathcal{V}''^{(0)} = \beta \int_{\mathbb{B}_\xi} \left\{ \frac{N_{11}^{(0)}}{\beta^2}\left(\frac{\partial \hat{w}^{(0)}}{\partial \xi_1}\right)^2 + N_{22}^{(0)}\left(\frac{\partial \hat{w}^{(0)}}{\partial \xi_2}\right)^2 + \frac{2N_{12}^{(0)}}{\beta}\frac{\partial \hat{w}^{(0)}}{\partial \xi_1}\frac{\partial \hat{w}^{(0)}}{\partial \xi_2} + \frac{D}{\beta^2 W^2}\left[\left(\frac{1}{\beta}\frac{\partial^2 \hat{w}^{(0)}}{\partial \xi_1^2} + \beta\frac{\partial^2 \hat{w}^{(0)}}{\partial \xi_2^2}\right)^2 - 2(1-\nu)\left(\frac{\partial^2 \hat{w}^{(0)}}{\partial \xi_2^2}\frac{\partial^2 \hat{w}^{(0)}}{\partial \xi_1^2} - \left(\frac{\partial^2 \hat{w}^{(0)}}{\partial \xi_1 \partial \xi_2}\right)^2\right)\right]\right\} \mathrm{d}\xi_1\,\mathrm{d}\xi_2, \tag{C.1}$$

$$\begin{aligned}\mathcal{V}''^{(1)} = \beta \int_{\mathbb{B}_\xi} \Bigg\{ & \frac{\partial \hat{w}^{(0)}}{\partial \xi_2}\left(N_{22}^{(1)}\frac{\partial \hat{w}^{(0)}}{\partial \xi_2} + 2N_{22}^{(0)}\frac{\partial \hat{w}^{(1)}}{\partial \xi_2}\right) + \frac{1}{\beta^2}\frac{\partial \hat{w}^{(0)}}{\partial \xi_1}\left[N_{11}^{(1)}\frac{\partial \hat{w}^{(0)}}{\partial \xi_1} + 2N_{11}^{(0)}\left(\frac{\partial \hat{w}^{(1)}}{\partial \xi_1} - \beta\frac{\partial \hat{w}^{(0)}}{\partial \xi_2}\right)\right] \\ & + 2\left[\frac{1}{\beta}\left(N_{12}^{(1)}\frac{\partial \hat{w}^{(0)}}{\partial \xi_2} + N_{12}^{(0)}\frac{\partial \hat{w}^{(1)}}{\partial \xi_2}\right)\frac{\partial \hat{w}^{(0)}}{\partial \xi_1} + N_{12}^{(0)}\frac{\partial \hat{w}^{(0)}}{\partial \xi_2}\left(\frac{1}{\beta}\frac{\partial \hat{w}^{(1)}}{\partial \xi_1} - \frac{\partial \hat{w}^{(0)}}{\partial \xi_2}\right)\right] \\ & + \frac{2D}{\beta^2 W^2}\left[\left(\frac{1}{\beta^2}\frac{\partial^2 \hat{w}^{(0)}}{\partial \xi_1^2} + \frac{\partial^2 \hat{w}^{(0)}}{\partial \xi_2^2}\right)\left(\frac{\partial^2 \hat{w}^{(1)}}{\partial \xi_1^2} + \beta^2\frac{\partial^2 \hat{w}^{(1)}}{\partial \xi_2^2} - 2\beta\frac{\partial^2 \hat{w}^{(0)}}{\partial \xi_1 \partial \xi_2}\right)\right. \\ & \left. -2(1-\nu)\left(\frac{\partial^2 \hat{w}^{(0)}}{\partial \xi_1^2}\frac{\partial^2 \hat{w}^{(1)}}{\partial \xi_2^2} + \frac{\partial^2 \hat{w}^{(0)}}{\partial \xi_2^2}\frac{\partial^2 \hat{w}^{(1)}}{\partial \xi_1^2} - 2\frac{\partial^2 \hat{w}^{(0)}}{\partial \xi_1 \partial \xi_2}\frac{\partial^2 \hat{w}^{(1)}}{\partial \xi_1 \partial \xi_2}\right)\right]\Bigg\} \mathrm{d}\xi_1\,\mathrm{d}\xi_2,\end{aligned} \tag{C.2}$$

and

$$\begin{aligned}\mathcal{V}''^{(2)} = \beta \int_{\mathbb{B}_\xi} \Bigg\{ & N_{11}^{(0)}\left[\left(\frac{1}{\beta}\frac{\partial \hat{w}^{(0)}}{\partial \xi_1} - \frac{\partial \hat{w}^{(0)}}{\partial \xi_2}\right)^2 + \frac{2}{\beta}\frac{\partial \hat{w}^{(0)}}{\partial \xi_1}\left(\frac{1}{\beta}\frac{\partial \hat{w}^{(2)}}{\partial \xi_1} - \frac{\partial \hat{w}^{(1)}}{\partial \xi_2}\right)\right] + N_{22}^{(0)}\left[\left(\frac{\partial \hat{w}^{(1)}}{\partial \xi_1}\right)^2 + 2\frac{\partial \hat{w}^{(0)}}{\partial \xi_2}\frac{\partial \hat{w}^{(2)}}{\partial \xi_2}\right] \\ & + 2N_{12}^{(0)}\left[\frac{1}{\beta}\frac{\partial \hat{w}^{(0)}}{\partial \xi_1}\frac{\partial \hat{w}^{(2)}}{\partial \xi_2} + \frac{\partial \hat{w}^{(1)}}{\partial \xi_2}\left(\frac{1}{\beta}\frac{\partial \hat{w}^{(1)}}{\partial \xi_1} - \frac{\partial \hat{w}^{(0)}}{\partial \xi_2}\right) + \frac{\partial \hat{w}^{(0)}}{\partial \xi_2}\left(\frac{1}{\beta}\frac{\partial \hat{w}^{(2)}}{\partial \xi_1} - \frac{\partial \hat{w}^{(1)}}{\partial \xi_2}\right)\right] + \frac{2}{\beta}N_{11}^{(1)}\frac{\partial \hat{w}^{(0)}}{\partial \xi_1}\left(\frac{1}{\beta}\frac{\partial \hat{w}^{(1)}}{\partial \xi_1} - \frac{\partial \hat{w}^{(0)}}{\partial \xi_2}\right) \\ & + 2N_{22}^{(1)}\frac{\partial \hat{w}^{(0)}}{\partial \xi_2}\frac{\partial \hat{w}^{(1)}}{\partial \xi_2} + 2N_{12}^{(1)}\left[\frac{1}{\beta}\frac{\partial \hat{w}^{(1)}}{\partial \xi_2}\frac{\partial \hat{w}^{(0)}}{\partial \xi_1} + \frac{\partial \hat{w}^{(0)}}{\partial \xi_2}\left(\frac{1}{\beta}\frac{\partial \hat{w}^{(1)}}{\partial \xi_1} - \frac{\partial \hat{w}^{(0)}}{\partial \xi_2}\right)\right] + \frac{1}{\beta^2}N_{11}^{(2)}\left(\frac{\partial \hat{w}^{(0)}}{\partial \xi_1}\right)^2 + N_{22}^{(2)}\left(\frac{\partial \hat{w}^{(0)}}{\partial \xi_2}\right)^2 \\ & + \frac{2}{\beta}N_{12}^{(2)}\frac{\partial \hat{w}^{(0)}}{\partial \xi_1}\frac{\partial \hat{w}^{(0)}}{\partial \xi_2} + \frac{D}{W^2\beta^2}\left[\left(\frac{1}{\beta}\frac{\partial^2 \hat{w}^{(1)}}{\partial \xi_1^2} + \beta\frac{\partial^2 \hat{w}^{(1)}}{\partial \xi_2^2} - 2\frac{\partial \hat{w}^{(0)}}{\partial \xi_1}\frac{\partial \hat{w}^{(0)}}{\partial \xi_2}\right)^2\right. \\ & + 2\left(\beta\frac{\partial^2 \hat{w}^{(0)}}{\partial \xi_2^2} + \frac{1}{\beta}\frac{\partial^2 \hat{w}^{(0)}}{\partial \xi_1^2}\right)\left(\beta\left(\frac{\partial^2 \hat{w}^{(0)}}{\partial \xi_2^2} + \frac{\partial^2 \hat{w}^{(2)}}{\partial \xi_2^2}\right) - 2\frac{\partial^2 \hat{w}^{(1)}}{\partial \xi_1 \partial \xi_2} + \frac{1}{\beta}\frac{\partial^2 \hat{w}^{(2)}}{\partial \xi_1^2}\right) + 2(1-\nu)\left(\left(\frac{\partial^2 \hat{w}^{(1)}}{\partial \xi_1 \partial \xi_2}\right)^2\right. \\ & \left.\left. + 2\frac{\partial^2 \hat{w}^{(0)}}{\partial \xi_1 \partial \xi_2}\frac{\partial^2 \hat{w}^{(2)}}{\partial \xi_1 \partial \xi_2} - \frac{\partial^2 \hat{w}^{(0)}}{\partial \xi_1^2}\frac{\partial^2 \hat{w}^{(2)}}{\partial \xi_2^2} - \frac{\partial^2 \hat{w}^{(1)}}{\partial \xi_1^2}\frac{\partial^2 \hat{w}^{(1)}}{\partial \xi_2^2} - \frac{\partial^2 \hat{w}^{(2)}}{\partial \xi_1^2}\frac{\partial^2 \hat{w}^{(0)}}{\partial \xi_2^2}\right)\right]\Bigg\} \mathrm{d}\xi_1\,\mathrm{d}\xi_2.\end{aligned} \tag{C.3}$$

Appendix D. Details of the derivation of the approximate in-plane stress solution, Eq. (57)

When the fields are described as functions of the auxiliary normalized coordinate $\boldsymbol{\xi}$, the stress - membrane force and the stress-strain (50) relations are preserved at the different orders

$$\boldsymbol{\sigma}^{(k)} = \frac{\mathbf{N}^{(k)}}{t} = \frac{E}{1-\nu^2}\left[\nu\ \mathrm{tr}\left(\boldsymbol{\epsilon}^{[m](k)}\right)\mathbf{I}_s + (1-\nu)\,\boldsymbol{\epsilon}^{[m](k)}\right], \qquad k = 1, 2, \tag{D.1}$$

but the strain-displacement relation (20) are transformed at the different orders into

$$\begin{Bmatrix} \epsilon_{11}^{[m](0)} \\ \epsilon_{12}^{[m](0)} \\ \epsilon_{22}^{[m](0)} \end{Bmatrix} = \frac{1}{W}\begin{Bmatrix} \frac{1}{\beta}\frac{\partial u_1^{(0)}}{\partial \xi_1} \\ \frac{1}{2}\left(\frac{\partial u_1^{(0)}}{\partial \xi_2} + \frac{1}{\beta}\frac{\partial u_2^{(0)}}{\partial \xi_1}\right) \\ \frac{\partial u_2^{(0)}}{\partial \xi_2} \end{Bmatrix}, \qquad \begin{Bmatrix} \epsilon_{11}^{[m](k)} \\ \epsilon_{12}^{[m](k)} \\ \epsilon_{22}^{[m](k)} \end{Bmatrix} = \frac{1}{W}\begin{Bmatrix} \frac{1}{\beta}\frac{\partial u_1^{(k)}}{\partial \xi_1} - \frac{\partial u_1^{(k-1)}}{\partial \xi_2} \\ \frac{1}{2}\left(\frac{\partial u_1^{(k)}}{\partial \xi_2} + \frac{1}{\beta}\frac{\partial u_2^{(k)}}{\partial \xi_1} - \frac{\partial u_2^{(k-1)}}{\partial \xi_2}\right) \\ \frac{\partial u_2^{(k)}}{\partial \xi_2} \end{Bmatrix}, \qquad k = 1, 2. \tag{D.2}$$

The second-order expansion for the stress field satisfying these relations, the indefinite equilibrium Eq. (54), and the boundary conditions (55) (with the integral boundary conditions (56) replacing Eqs. $(55)_7$ and $(55)_8$) is found to be provided by the following closed-form polynomial expressions in the auxiliary coordinates ξ_1 and ξ_2

$$\begin{Bmatrix} \sigma_{11}(\boldsymbol{\xi}) \\ \sigma_{12}(\boldsymbol{\xi}) \\ \sigma_{22}(\boldsymbol{\xi}) \end{Bmatrix} = E\,\epsilon\left(\begin{Bmatrix} 1 \\ 0 \\ 0 \end{Bmatrix} + \theta_0\begin{Bmatrix} -12\beta\xi_1\xi_2 \\ -\frac{1}{2} + 6\xi_2^2 \\ 0 \end{Bmatrix} + \theta_0^2\begin{Bmatrix} 1 + \frac{\beta^2 - 3\nu}{2} - 24\xi_2^2 - C \\ -12\beta\xi_1\xi_2 \\ -2 + 12\xi_2^2 \end{Bmatrix}\right), \qquad \boldsymbol{\xi} \in \mathbb{B}_{\boldsymbol{\xi}}. \tag{D.3}$$

This solution can be finally projected onto the parallelogram domain $\mathbb{B}_{\mathbf{x}}$ through the expanded linear transformation (53), leading to Eq. (57).

References

Barber, J.R., 2002. Elasticity. Springer.
Bigoni, D., Bosi, F., Dal Corso, F., Misseroni, D., 2014. Instability of a penetrating blade. J. Mech. Phys. Solids 64, 411–425.
Bosi, F., Misseroni, D., Dal Corso, F., Neukirch, S., Bigoni, D., 2016. Asymptotic self-restabilization of a continuous elastic structure. Phys. Rev. E 94 (6), 063005.
Brojan, M., Terwagne, D., Lagrange, R., Reis, P.M., 2015. Wrinkling crystallography on spherical surfaces. Proc. Nat. Acad. Sci. 112 (1), 14–19.
Calladine, C.R., 1983. Theory of Shell Structures. Cambridge University Press.
Cerda, E., Mahadevan, L., 2003. Geometry and physics of wrinkling. Phys. Rev. Lett. 90 (7), 074302.
Cerda, E., Ravi-Chandar, K., Mahadevan, L., 2002. Wrinkling of an elastic sheet under tension. Nature 419 (6907), 579–580.
Chai, P.-P., Liu, Y., Wang, F.F., 2024. Stretch-induced wrinkling of anisotropic hyperelastic thin films. Thin-Walled Structures 200, 111961.
Coman, C.D., 2007. On the applicability of tension field theory to a wrinkling instability problem. Acta Mech. 190 (1), 57–72.
Coman, C.D., 2023. Wrinkling of a normally loaded, spinning, elastic membrane: an asymptotic approximation. Int. J. Non Linear Mech. 156, 104482.
Coman, C.D., Bassom, A.P., 2016. On the nonlinear membrane approximation and edge-wrinkling. Int. J. Solids Struct. 82, 85–94.
Comitti, A., Vijayakumaran, H., Nejabatmeimandi, M.H., Seixas, L., Cabello, A., Misseroni, D., Penasa, M., Paech, C., Bessa, M., Bown, A.C., Dal Corso, F., Bosi, F., 2024. Ultralight Membrane Structures Toward a Sustainable Environment. Springer International Publishing, Cham. pp. 17–37.
Damil, N., Potier-Ferry, M., Hu, H., 2013. New nonlinear multi-scale models for wrinkled membranes. Comptes Rendus Mécanique 341 (8), 616–624.
Danielson, D.A., Natarajan, S., 1975. Tension field theory and the stress in stretched skin. J. Biomech. 8 (2), 135–142.
Destrade, M., Fu, Y., Nobili, A., 2016. Edge wrinkling in elastically supported pre-stressed incompressible isotropic plates. Proc. R. Soc. A: Math. Phys. Eng. Sci. 472 (2193), 20160410.
Ding, M., Xu, F., Wang, T., Fu, C., 2021. Nanosleeves: morphology transitions of infilled carbon nanotubes. J. Mech. Phys. Solids 152, 104398.
Fehér, E., Healey, T.J., Sipos, A.A., 2018. The Mullins effect in the wrinkling behavior of highly stretched thin films. J. Mech, Phys. Solids 119, 417–427.
Friedl, N., Rammerstorfer, F.G., Fischer, F.D., 2000. Buckling of stretched strips. Comput. Struct. 78 (1–3), 185–190.
Friesecke, , G., James, , R., Müller, S., 2006. A hierarchy of plate models derived from nonlinear elasticity by gamma-convergence. Arch. Rational Mech. Anal. 180, 183–236.
Fu, C., Dai, H.-H., Xu, F., 2021. Computing wrinkling and restabilization of stretched sheets based on a consistent finite-strain plate theory. Comput. Methods Appl. Mech. Eng. 384, 113986.
Fu, C., Wang, T., Xu, F., Huo, Y., Potier-Ferry, M., 2019. A modeling and resolution framework for wrinkling in hyperelastic sheets at finite membrane strain. J. Mech. Phys. Solids 124, 446–470.
Fu, C., Yang, Y., Wang, T., Xu, F., 2022. A consistent finite-strain plate model for wrinkling of stretched anisotropic hyperelastic films. Thin-Walled Struct. 179, 109643.
Healey, T.J., Li, Q., Cheng, R.B., 2013. Wrinkling behavior of highly stretched rectangular elastic films via parametric global bifurcation. J. Nonlinear Sci. 23, 777–805.
Hilgers, M.G., Pipkin, A.C., 1992. Bending energy of highly elastic membranes. Q. Appl. Math. 50(2), 389–400.
Hilgers, M.G., Pipkin, A.C., 1996. Bending energy of highly elastic membranes II. Q. Appl. Math. 54(2), 307–316.
Hure, J., Roman, B., Bico, J., 2012. Stamping and wrinkling of elastic plates. Phys. Rev. Lett. 109 (5), 054302.
Ishida, T., Matsubara, S., Nagashima, S., Okumura, D., 2024. Deformation in the wrinkle–crease transformation. Int. J. Solids Struct. 298, 112876.
Jacques, N., Potier-Ferry, M., 2005. On mode localisation in tensile plate buckling. Comptes rendus. Mécanique 333 (11), 804–809.
Jiménez, F.L., Stoop, N., Lagrange, R., Dunkel, J., Reis, P.M., 2016. Curvature-controlled defect localization in elastic surface crystals. Phys. Rev. Lett. 116 (10), 104301.
Kim, T.-Y., Puntel, E., Fried, E., 2012. Numerical study of the wrinkling of a stretched thin sheet. Int. J. Solids Struct. 49 (5), 771–782.
Kossa, A., Valentine, M.T., McMeeking, R.M., 2023. Analysis of the compressible, isotropic, neohookean hyperelastic model. Meccanica 58, 217–232.
Lagrange, R., Jiménez, F.L., Terwagne, D., Brojan, M., Reis, P.M., 2016. From wrinkling to global buckling of a ring on a curved substrate. J. Mech. Phys. Solids 89, 77–95.
Landis, C.M., Huang, R., Hutchinson, J.W., 2022. Formation of surface wrinkles and creases in constrained dielectric elastomers subject to electromechanical loading. J. Mech. Phys. Solids 167, 105023.
Li, Q., Healey, T.J., 2016. Stability boundaries for wrinkling in highly stretched elastic sheets. J. Mech. Phys. Solids 97, 260–274.

Liu, F., Xu, F., Fu, C., 2019. Orientable wrinkles in stretched orthotropic films. Extreme Mech. Lett. 33, 100579.
Migliaccio, G., D'Annibale, F., 2025. On the inadequacy of a stepped-beam approach in predicting shear stresses in tapered slender solids. Eur. J. Mech.-A/Solids 111, 105590.
Migliaccio, G., Ruta, G., 2020. Rotor blades as curved, twisted and tapered beam-like structures subjected to large deflections. Eng. Struct. 222, 111089.
Mirandola, A., Cutolo, A., Carotenuto, A.R., Nguyen, N., Pocivavsek, L., Fraldi, M., Deseri, L., 2023. Toward new scaling laws for wrinkling in biologically relevant fiber-reinforced bilayers. J. Appl. Phys. 134, 154702.
Misseroni, M., Pratapa, P.P., Liu, K., Paulino, G.H., 2022. Experimental realization of tunable poisson's ratio in deployable origami metamaterials. Extreme Mech. Lett. 53, 101685.
Nardinocchi, P., Puntel, E., 2017. Swelling-induced wrinkling in layered gel beams. Proc. R. Soc. A: Math. Phys. Eng. Sci. 473 (2207), 20170454.
Nayyar, V., Ravi-Chandar, K., Huang, R., 2011. Stretch-induced stress patterns and wrinkles in hyperelastic thin sheets. Int. J. Solids Struct. 48 (25–26), 3471–3483.
Pipkin, A.C., 1986. The relaxed energy density for isotropic elastic membranes. IMA J. Appl. Math. 36 (1), 85–99.
Plucinsky, P., Bhattacharya, K., 2017. Microstructure-enabled control of wrinkling in nematic elastomer sheets. J. Mech. Phys. Solids 102, 125–150.
Puntel, E., Deseri, L., Fried, E., 2011. Wrinkling of a stretched thin sheet. J. Elast. 105, 137–170.
Reissner, E., 1938. On tension field theory. Proc. of the 5th Int. Congr. for Appl. Mech. Harvard Univ. & MIT , 88–92.
Shen, J., Fu, Y., Pirrera, A., Groh, R.M.J., 2024. Wrinkling of differentially growing bilayers with similar film and substrate moduli. J. Mech. Phys. Solids 193, 105900.
Sipos, A.A., Fehér, E., 2016. Disappearance of stretch-induced wrinkles of thin sheets: a study of orthotropic films. Int. J. Solids Struct. 97, 275–283.
Steigmann, D.J., 1990. Tension-field theory. Proc. R. Soc. London. A. Math. Phys. Sci. 429 (1876), 141–173.
Steigmann, D.J., 2013. Koiter's shell theory from the perspective of three-dimensional nonlinear elasticity. J. Elast. 111, 91–107.
Stein, M., Hedgepeth, J.M., 1961. Analysis of Partly Wrinkled Membranes. National Aeronautics and Space Administration.
Stoop, N., Lagrange, R., Terwagne, D., Reis, P.M., Dunkel, J., 2015. Curvature-induced symmetry breaking determines elastic surface patterns. Nat. Mater. 14 (3), 337–342.
Suñé, M., Arratia, C., Bonfils, A.F., Vella, D., Wettlaufer, J.S., 2023. Wrinkling composite sheets. Soft Matter 19 (45), 8729–8743.
Taylor, M., Bertoldi, K., Steigmann, D.J., 2014. Spatial resolution of wrinkle patterns in thin elastic sheets at finite strain. J. Mech. Phys. Solids 62, 163–180.
Timoshenko, S., Woinowsky-Krieger, S., 1959. Theory of Plates and Shells. Mc Graw-Hill.
Vandeparre, H., Piñeirua, M., Brau, F., Roman, B., Bico, J., Gay, C., Bao, W., Lau, C.N., Reis, P.M., Damman, P., 2011. Wrinkling hierarchy in constrained thin sheets from suspended graphene to curtains. Phys. Rev. Lett. 106 (22), 224301.
Venkata, S.P., Balbi, V., Destrade, M., Accoto, D., Zurlo, G., 2023. Programmable wrinkling for functionally-graded auxetic circular membranes. Extreme Mech. Lett. 63, 102045.
Wagner, H., 1929. Flat sheet metal girders with very thin metal web. Z. flugtechn. motorluftschiffahrt 20, 200–314.
Wang, F.-F., Wang, T., Zhang, X., Huang, Y., Giorgio, I., Xu, F., 2023. Wrinkling of twisted thin films. Int. J. Solids Struct. 262, 112075.
Wang, T., Fu, C., Potier-Ferry, M., Xu, F., 2024. Morphomechanics of growing curled petals and leaves. J. Mech. Phys. Solids 184, 105534.
Wang, T., Fu, C., Xu, F., Huo, Y., Potier-Ferry, M., 2019. On the wrinkling and restabilization of highly stretched sheets. Int. J. Eng. Sci. 136, 1–16.
Wang, T., Potier-Ferry, M., Xu, F., 2025. A nonlinear toroidal shell model for surface morphologies and morphogenesis. J. Mech. Phys. Solids 200, 106135.
Wang, T., Yang, Y., Fu, C., Liu, F., Wang, K., Xu, F., 2020. Wrinkling and smoothing of a soft shell. J. Mech. Phys. Solids 134, 103738.
Wang, T., Yang, Y., Xu, F., 2022. Mechanics of tension-induced film wrinkling and restabilization: a review. Proce. R. Soc. A 478 (2263), 20220149.
Wong, W., Pellegrino, S., 2006a. Wrinkled membranes i: experiments. J. Mech. Mater. Struct. 1 (1), 3–25.
Wong, W., Pellegrino, S., 2006b. Wrinkled membranes III: numerical simulations. J. Mech. Mater. Struct. 1 (1), 63–95.
Xu, F., Potier-Ferry, M., 2016. On axisymmetric/diamond-like mode transitions in axially compressed core–shell cylinders. J. Mech. Phys. Solids 94, 68–87.
Xu, F., Potier-Ferry, M., Belouettar, S., Hu, H., 2015. Multiple bifurcations in wrinkling analysis of thin films on compliant substrates. Int. J. Non Linear Mech. 76, 203–222.
Xu, F., Wang, T., Fu, C., Cong, Y., Huo, Y., Potier-Ferry, M., 2017. Post-buckling evolution of wavy patterns in trapezoidal film/substrate bilayers. Int. J. Non Linear Mech. 96, 46–55.
Yang, E., Zhang, M., Zeng, J., Tian, F., 2022. Wrinkling and restabilization of a hyperelastic PDMS membrane at finite strain. Soft Matter 18 (29), 5465–5473.
Zheng, L., 2009. Wrinkling of Dielectric Elastomer Membranes. California Institute of Technology.